INVITED PAPER

Revolution of Electric Vehicle Charging Technologies Accelerated by Wide Bandgap Devices

This article reviews wide bandgap devices (WBGs) and their impact on the development of electric vehicle charging equipment.

By SIQI LI, *Member IEEE*, SIZHAO LU, *Member IEEE*, AND CHUNTING CHRIS MI, *Fellow IEEE*

ABSTRACT | This article presents the state-of-the-art electric vehicle (EV) charging technologies that benefit from the wide bandgap (WBG) devices, which is regarded as the most significant revolution in the power electronics industry in the past few decades. First, the recent WBG device technology evolution, performance comparison, and reliability issues are introduced. Then, topology development, efficiency and power density boost, and cost reduction brought by the WBG devices for EV charging equipment, such as onboard chargers, fast-charging stations, and wireless chargers, are discussed. A figure of merit (FOM) for evaluating the performance of wireless chargers is also proposed. Finally, the EV charging technology roadmap forecast is presented based on the WBG devices' evolutionary trends.

KEYWORDS | Electric vehicle (EV); fast charger; onboard charger (OBC); wide bandgap (WBG) devices; wireless power transfer (WPT).

NOMENCLATURE

EVs	Electric vehicles.
OBC	Onboard charger.
SAE	Society of Automotive Engineers.
SOC	State of charge.
WBG	Wide bandgap.
SiC	Silicon carbide.
GaN	Gallium nitride.
SBD	Schottky barrier diode.
2DEG	2-D electron gas.
MOSFETs	Metal–oxide–semiconductor field-effect transistors.
JFETs	Junction field-effect transistors.
HEMT	High electron mobility transistor.
E-HEMT	Enhancement HEMT.
IGBT	Insulated gate bipolar transistor.
GTO	Gate turn-off thyristor.
PFC	Power factor correction.
DNPC	Diode neutral-point-clamped converter.
MV	Medium voltage.
SST	Solid-state-transformer.
IPT	Inductive power transfer.
CPT	Capacitive power transfer.
WPTFOM	Figure of merit for a WPT system.

Manuscript received August 12, 2020; revised March 3, 2021; accepted April 2, 2021. Date of publication April 26, 2021; date of current version May 20, 2021. *(Corresponding author: Chunting Chris Mi.)*

Siqi Li and **Sizhao Lu** are with the Department of Electrical Engineering, Kunming University of Science and Technology, Kunming 650500, China (e-mail: lisiqi@kust.edu.cn; lusz10@kust.edu.cn).

Chunting Chris Mi is with the Department of Electrical and Computer Engineering, San Diego State University, San Diego, CA 92182 USA (e-mail: mi@ieee.org).

Digital Object Identifier 10.1109/JPROC.2021.3071977

I. INTRODUCTION

Compared with traditional fossil fuel vehicles, the advantages of EVs in energy saving, environmental friendliness, and acceleration performance have made them prosper in recent years. Besides the cost aspect, range anxiety is a major consideration by pure EV users [1]. Fast, efficient, and convenient charging is very important for the further penetration of EVs. EVs are usually equipped with an OBC. In the United States, when the charger is connected to a convenient 120-V outlet, the charging rate will be limited to Level 1 power as defined in SAE standard J1772 [2]. The maximum charging power is 1.92 kW as per Level 1 profile. When there is a dedicated EV supply equipment (EVSE)

or a 208-V/240-V outlet, the output power of the OBC can be increased to Level 2 for semifast charging with the maximum allowable charging power up to 19.2 kW. The power of an OBC is limited by cost, volume, and weight constraints in a vehicle. Most original preinstalled OBC for light-duty vehicles (LDVs) is far below 19.2 kW. Chevrolet Bolt EV has a 7.2-kW OBC [3]. The power of Tesla Model 3 and Model S OBC ranges from 7.6 to 11.5 kW [4]. With a level 2 OBC, the miles of range for an EV can be restored at a rate of 20–50 km/h, which means that it will take approximately 10 h to obtain a cruising range similar to that of an internal combustion engine car. There is an urgent need for charging power of tens to hundreds of kilowatts to replenish a considerable cruising range in a few minutes; thus, the range anxiety can be alleviated. Fast or ultrafast dc charging equipment, which can provide a dc current directly to the battery, has been developed to meet the demand. The SAE J1772 defines two dc fast-charging power levels: dc Level 1 and dc Level 2. The maximum power of dc Level 1 is 80 kW, and the maximum power of dc Level 2 is 400 kW. There are also a few other competing dc fast-charging standards, such as CHAdeMO, Tesla supercharger, and GB/T 20234.3. Tesla has achieved the 145-kW output capability of its supercharger v2 in 2019. The latest supercharger v3 has a maximum charging power of 250 kW. Considering that most of Tesla's battery pack capacity ranges from 75 kW to 100 kWh, the maximum charging rate will be higher than 2 C. However, the allowable charging rate is inversely proportional to the SOC of the battery [5]. When the SOC increases, the charging power decreases linearly. The maximum power cannot be maintained during the entire charging process, which will significantly increase the charging time. It usually takes about 30–60-min recharge time to reach 80% SOC for most EVs using fast-charging stations.

Wireless charging has also gained special consideration due to its convenience and safety. The SAE released the recommended practices for EV wireless charging SAE J2954 in 2016 and made two rounds of revisions in 2017 and 2019. China also published its latest wireless charging standard GB/T 38775 in May 2020. In 2018, BMW has announced its inductive wireless charging program for the plug-in hybrid sedan. In June 2020, Momentum Dynamics and Jaguar Land Rover together initiated the wireless charging electric taxi program in Oslo, Norway. Dynamic online wireless charging can also reduce the battery capacity, thereby greatly reducing the cost of EVs, but requires a substantial investment in road infrastructure [6].

Fig. 1 shows the current number of EVs and charging infrastructure. Battery EVs (BEVs) and plug-in hybrid EVs (PHEVs) are growing rapidly every year. It is estimated that, by 2025, the number of EVs will increase to 50–80 million. By 2030, it will increase to 140–245 million, which is more than 20 times that of 2019 [7]. The continuously increasing EVs have brought a strong demand for improvement of charging technology.

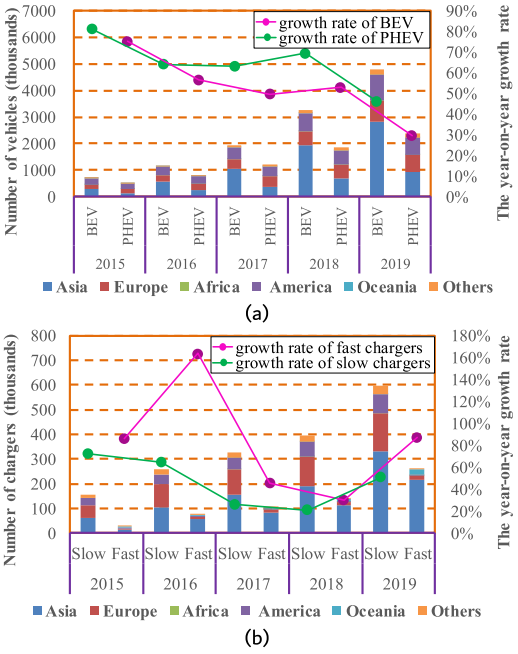

Fig. 1. ***Growth trends of EVs and charging infrastructures (data extracted from [7]). (a) EVs (BEV and PHEV). (b) Publicly accessible chargers.***

Whether the charging device is on the ground or on the vehicle, wired or wireless, the energy conversion efficiency is of paramount importance. For the large number of EVs, even a slight improvement in efficiency can save a significant amount of energy. More importantly, the high efficiency in high-power applications is conducive to the size and cost reduction of the passive components and cooling systems; thus, the overall power density can be significantly improved [8]. In addition to efficiency and cost, power density and reliability are more valued on the vehicle side, while, on the ground side, cost and power capacity are more important considerations. Technologies related to EV charging equipment are constantly evolving to improve efficiency, power density, and power capacity while reducing costs. New topologies, pulsewidth modulation strategies, magnetic materials, and semiconductor power devices are the source of technological advancement in charging equipment. Among the above, power semiconductor devices are the most basic and key technologies that determine and influence the evolution of all other peripheral technologies. Their performance and characteristics play a decisive role in the efficiency and power density of EV charging equipment. Traditional silicon-based power semiconductors have already reached their theoretical limits after a few decades of development [9]. The WBG material, which has a relatively larger energy gap between the conduction band and the valence band, is considered to be a new generation of materials that can greatly improve the performance of power semiconductor devices. The performance of the first generation

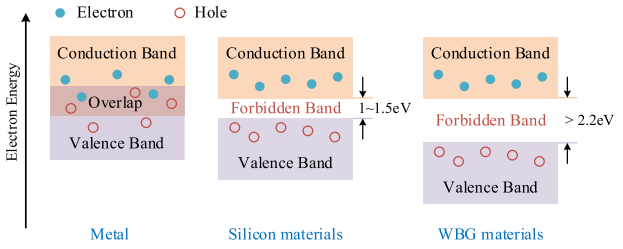

Fig. 2. ***Material energy bands.***

of WBG devices, such as the very early design of SiC MOSFET [10], has broken through the theoretical limit of silicon devices. A high-power-density battery charger with 97% efficiency has already been developed using WBG devices [11].

In the past two decades, the WBG wafer fabrication processes have continued to develop, and the performance has improved, while the cost has dropped significantly. More and more WBG devices have been used and introduced in research projects and mass productions. The following sections will introduce the evolution from WBG devices to EV charging technology over the past few decades.

II. OVERVIEW AND STATE-OF-THE-ART WBG DEVICES

A. Material Basics

For all materials, there are conduction bands and valence bands, as shown in Fig. 2. When the electrons in the valence band jump to the conduction band forming free electrons, the material will exhibit conductive properties. For semiconductor materials, there is an obvious energy gap between the conduction band and the valence band. This energy gap is also called the forbidden band. Generally, semiconductor materials with an energy bandgap greater than 2.2 eV are called WBG materials [12].

Due to the WBG, the intrinsic carrier density is much lower than that of silicon. The low intrinsic carrier density ensures high-temperature operation, low reverse recovery, and low leakage current. The breakdown field characterizes the dielectric strength of the material. The high breakdown field makes WBG devices more competitive in high-voltage and high-power devices. Also, a high breakdown field means thinner layer thickness or shorter channel length to block the high voltage, ensuring a low ON-resistance. High electron mobility is also beneficial for achieving low ON-resistance. Thermal conductivity determines heat dissipation capability, which is essential for the power density of the device.

The most highly touted WBG materials for now and the near future are SiC and GaN. There are more than 200 recognized polytypes of SiC, among which 3C-SiC, 6H-SiC, and 4H-SiC are the most commonly studied. 4H-SiC is superior to 3C-SiC in terms of critical electric field strength, and the mobility anisotropy is much smaller than that of 6H-SiC. With the development of single-crystal wafer growth methods, 4H-SiC has become the most suitable and almost exclusive material for power device applications [12]. Unless otherwise specified, all SiCs will represent 4H-SiC hereafter.

To evaluate the semiconductor material performance, various definitions of the figure of merit (FOM) have been proposed. In 1965, Johnson FOM (JFOM) was derived by defining the power–frequency product, which represents a transistor's voltage–ampere, power gain, and frequency performance [13]. In 1982, Baliga FOM (BFOM) was proposed, which represents the power-handling capability per unit area of a power device[14]. In 2004, Huang [15] proposed three new FOMs, among which the Huang material FOM (HMFOM) takes the switching losses into consideration and is inversely proportional to the material minimum power loss. The JFOM, BFOM, and HMFOM values are given in Table 1. Under all definitions, SiC and GaN materials have much higher FOMs than that of Si. As the fabrication matures, the performance revolution of power semiconductor devices is advancing rapidly to achieve the full potential of WBG materials.

B. Wafer Fabrication and Cost

The material wafer substrate is the starting point for manufacturing power semiconductor devices. Larger and high-quality wafers are required for the commercialization of WBG devices. For the last two silicon wafer size transitions, from 150 to 200 mm and from 200 to 300 mm, the cost per chip area of silicon-based devices has been reduced by approximately 30% each time. Therefore, in the past two decades, how to make larger WBG wafers with low defects has always been a hot research topic.

In 1997, Cree, a leading SiC power device company, developed a high-quality 50-mm SiC wafer with micropipe density as low as 1.1 cm^{-2} [19]. In the next few years, 75- and 100-mm SiC wafers were developed by Infineon and Cree, respectively [20]. In 2010, high-quality 150-mm SiC wafers were developed by Cree. In 2015, 200-mm SiC wafers were demonstrated by both Wolfspeed [21]

Table 1 Material Properties and FOM Comparison [16]–[18]

Properties and FOM* \ Materials	Si	4H-SiC	GaN
Bandgap energy E_g (eV)	1.1	3.26	3.39
Critical electric field E_c (MV/cm)	0.3	2.0	3.3
Electron mobility μ (cm^2/V·s)	1350	720^a/650^c	900
Saturation drift velocity v_s	1.0	2.0	2.5
Relative dielectric constant ε	11.8	10	9.0
Thermal conductivity λ	1.5	4.5	1.3
JFOM* = $E_c \cdot v_s / 2\pi$	1.0	13.3	27.5
BFOM* = $\varepsilon \cdot \mu \cdot E_c^3$	1.0	133.9	676.8
HMFOM* = $E_c \cdot \sqrt{\mu}$	1.0	4.87	8.98

Note: * – All FOM data are normalized against silicon, ^{a} – mobility along *a*-axis, ^{c} – mobility along *c*-axis

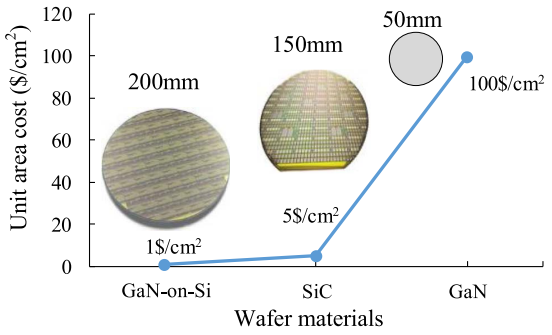

Fig. 3. ***Commercialized WBG wafers and their unit area cost [32], [33].***

(rebranding from Cree's power and RF division) and II–VI Incorporated [22]. As the 150-mm SiC wafer manufacturing process matures, the price of commercial SiC devices has decreased by 80% compared to ten years ago. When switching to 200-mm wafers in the near future, the price of SiC may be reduced to half of the current price, which means that the SiC devices will cost only 1.5 times that of Si devices with the same ratings [23].

Compared with SiC, the progress in the manufacturing process of GaN wafers is relatively slow. In 1998, Kim *et al.* [24] have grown a thick GaN wafer on a sapphire substrate using the hydride vapor phase epitaxy (HVPE) method. Then, the sapphire substrate was removed to obtain a 10 mm $\times$ 10 mm free-standing GaN substrate [24]. Later, in 2000, a 50-mm GaN wafer was fabricated also using the HVPE method [25]. In 2013, a 100-mm GaN wafer was reported using the HVPE method [26]. In 2017, a 175-mm GaN wafer was first fabricated using a tiling method together with HVPE by SCIOCS [27]. HVPE has become the most popular method for the epitaxial growth of GaN wafers. Although the larger size and lower dislocation GaN wafers have been obtained in the laboratory, there is no existing tool for mass production, which makes the cost of GaN wafers high. In 2018, the cost of a 50-mm GaN wafer is about \$2,000, and the cost of a 150-mm SiC wafer is about \$900 [28]. It means that the cost per unit area of GaN wafers is about 20 times that of SiC wafers. The fabrication difficulties of GaN wafers lead to enormous disparity in actual device performance and theoretical material characteristics. To take advantage of GaN materials, an alternative way is using a GaN-on-Si substrate. Various methods of heteroepitaxial growth of GaN materials on silicon wafers are proposed [29]. An attractive point is that GaN-on-Si wafers are compatible with the production lines commonly used in the semiconductor industry. Thus, GaN-on-Si substrates of 150 to 200 mm are very cost-effective as they can be manufactured using existing depreciated silicon fabricating facilities [30]. In 2018, the cost of 200-mm GaN-on-Si wafers was less than \$1/cm^2, which means that the cost per unit area was only 1/5 of SiC wafers [31]. The comparison of different WBG wafer sizes and unit area costs is given in Fig. 3. In contrast, the price per square centimeter of a 300-mm Si wafer is about \$0.5. The wafer cost of WBG and Si materials has become very close. The use of WBG devices as the key devices in high-performance EV charging applications is already affordable.

C. Devices Structures and Performance

1) WBG Diodes: Since the manufacture of SiC bulk wafers is very mature, the vertical structure of SiC diodes suitable for power applications is usually adopted. The basic structures of SiC diodes are no different from Si diodes, as shown in Fig. 4. For the structure of Schottky in Fig. 4(a), the N-epitaxial layer forms a Schottky contact with the anode metal, which brings a low forward voltage drop and a fast reverse recovery process to the SBD. In multikilovolt high-voltage applications, the SiC p-i-n structure is usually adopted, as shown in Fig. 4(b). The p-i-n structure adds an additional N-layer to the traditional p-n diodes. Due to the high critical electric field strength of SiC, the drift region is much thinner than that of Si p-i-n diodes. This means that much less charge is stored in the drift region, which is conducive to high switching speed and fast reverse recovery. As a bipolar device, the conductivity modulation effect of the SiC p-i-n diode can maintain a low ON-resistance even at high current densities. The downside of the SiC p-i-n diode is its higher ON-state voltage drop due to the large energy bandgap. Fig. 4(c) shows the junction barrier Schottky (JBS) or merged p-i-n Schottky (MPS) structure, which is composed of a Schottky part and a p-i-n part in parallel. It combines the structure of Schottky and p-i-n diodes and takes the advantage of both [34]. Due to the addition of P+ pitches, the voltage blocking capacity of a JBS diode is about 20% higher than an SBD diode with the same epitaxial layer [35]. The SBD and JBS/MPS diode are suitable for 600$\sim$3300-V applications, while the p-i-n diodes are for even higher voltage. As an example, a 21.7-kV SiC p-i-n diode was fabricated and tested in 2012 [36].

Once the substrate and epitaxial layers in Fig. 4 are replaced by corresponding GaN materials, GaN diodes can be realized. GaN power devices fabricating on native bulk GaN substrates are called GaN-on-GaN devices [37]. Although the performance of GaN-on-GaN devices is very attractive, the cost of free-standing GaN wafers is too high.

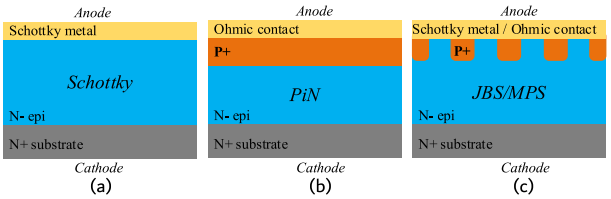

Fig. 4. ***SiC diodes structures. (a) Schottky. (b) p-i-n. (c) JBS/MPS.***

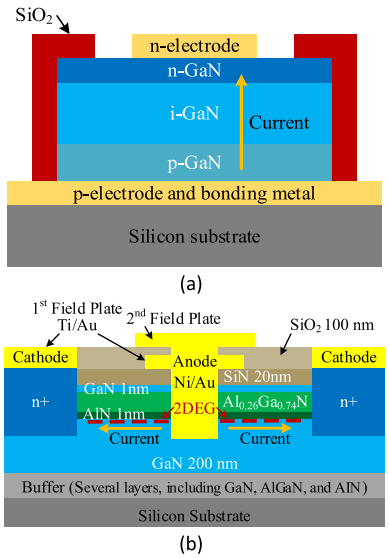

Fig. 5. *GaN diodes structures. (a) Vertical p-i-n [38]. (b) Lateral Schottky [39].*

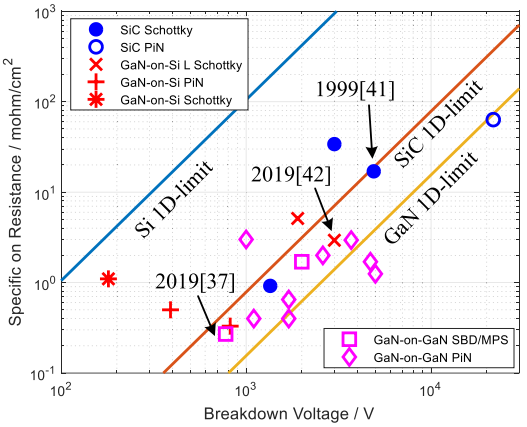

Fig. 6. *R_{onsp} versus breakdown voltage of WBG diodes.*

Considering the cost issues, diodes based on GaN-on-Si wafers have been studied recently. There are two basic configurations of GaN-on-Si diodes. One is the vertical structure, as shown in Fig. 5(a). The GaN-on-Si diodes also have a lateral form, as shown in Fig. 5(b). A 2DEG is generated at the heterojunction of the AlN and GaN layers. Due to the high electron mobility in the 2DEG, high conductivity can be realized between the anode and the cathode.

2) WBG Diodes' Performance: The relationship between specific ON-resistance R_{onsp}, which is the ON-resistance per unit wafer area, and the breakdown voltage V_B is usually used to evaluate the conduction performance of a power device. The theoretical R_{onsp} limit of the material can be calculated as

$$R_{\text{onsp}} = \frac{4V_B^2}{\mu\varepsilon E_c^3} \tag{1}$$

where μ is the electron mobility, ε is the relative dielectric constant, and E_c is the critical electric field. It is derived using the unipolar 1-D device model [40]. Fig. 6 shows the performance statistics of recent SiC and GaN diodes. The theoretical R_{onsp} of SiC and GaN diodes are two to three orders lower than that of the silicon diodes, which means a great potential in loss reduction and efficiency improvement. As early as 1999, the reported SiC Schottky diode had reached the theoretical material limit [41]. With the maturity of SiC wafer fabrications, SiC Schottky diodes have already been commercialized and widely used in EV high-performance chargers. In the case of GaN diodes, the recently reported GaN-on-Si lateral SBD [42] and GaN-on-GaN SBD [37] are still far from the material limit. However, the GaN-on-Si Schottky diodes have already exceeded the SiC limits. Considering the maturity and low cost of GaN-on-Si wafers, it is quite possible that the GaN-on-Si lateral SBD is commercialized in the near future.

The ON-resistance of the bipolar p-i-n diodes can be much smaller than the 1-D limit due to the conductivity modulation. The respective unipolar device limits have been broken by both the SiC and GaN p-i-n diodes [43]. One drawback of the p-i-n diode is that its initial turn-on voltage drop and switching losses are much higher than those of SBD. The WBG p-i-n diode is more suitable for high-voltage high-power and relatively low switching frequency applications.

Fig. 7 demonstrates the switching performance of the WBG diodes compared with Si diodes. In Fig. 7(a), the reverse recovery current of a 4.5-kV SiC JBS is less than 1/5 of a Si 4.5-kV p-i-n diode. Also, the reverse recovery time is significantly shorter than the Si p-i-n diode. In Fig. 7(b), a vertical GaN-on-Si p-i-n diode is compared with a commercial fast recovery silicon diode UF4004. The reverse recovery current of the GaN diode is only 1/7 that of the comparative diode. In addition, the switching characteristics of GaN diodes remain almost unchanged over a wide temperature range.

3) Unipolar WBG Power Transistors: MOSFET and JFET are two common types of unipolar transistors, which use

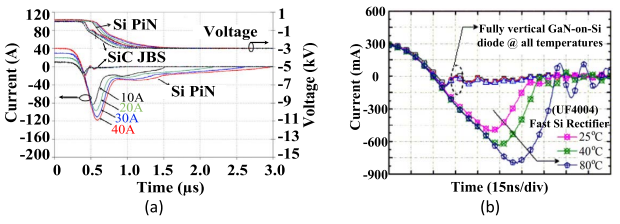

Fig. 7. *Diodes reverse recover current comparison. (a) 4.5-kV Si p-i-n versus SiC JBS [44]. (b) GaN-on-Si versus ultrafast Si [38].*

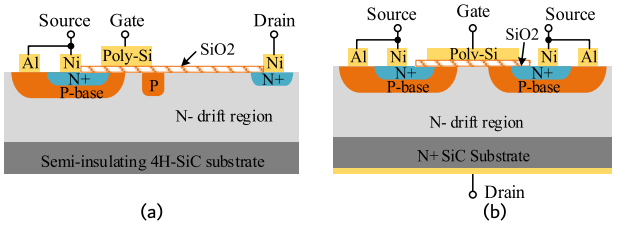

Fig. 8. *SiC MOSFET structures. (a) Lateral MOSFETs [45]. (b) Vertical MOSFETs [46].*

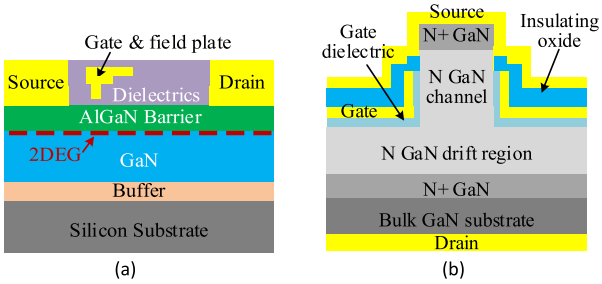

Fig. 10. *Typical GaN Structures [30]. (a) Lateral GaN HEMT. (b) Vertical GaN Fin FET.*

only majority carriers to conduct current. SiC has SiO_2 as its native and stable oxide, which is essential for fabricating SiC MOSFET. Research and commercialization of SiC MOSFETs have made considerable progress with the development of SiC wafer manufacturing technology. When the reverse blocking voltage is not too high, the lateral structure, as shown in Fig. 8(a), can be used. The gate, drain, and source terminals of the lateral SiC MOSFET can be configured on the top surface, which is particularly suitable for monolithic integration with other circuits.

The vertical structure of the SiC MOSFETs shown in Fig. 8(b) is preferable for high-voltage and high-power applications. Since its structure is not much different from that of silicon MOSFET, the development of SiC MOSFET is very rapid. The performance of the vertical structure SiC MOSFET is very close to its theoretical limit [47]. There are already many cost-effective SiC MOSFETs on the market. Manufacturers such as Infineon, Wolfspeed, and ROHM are offering on-the-shelf SiC MOSFETs from 600- to 1700-V voltage ratings.

SiC can also be made into corresponding JFET devices. Compared with MOSFET, JFET has the advantages of low ON-resistance and high reliability. However, its main disadvantage is that it can only work in the depletion mode, which means that JFET is a normally-on device [48]. For power electronics applications, it is undesirable to have an ON-state JFET before applying the control power. As a solution, a low-voltage Si MOSFET is usually connected to the SiC JFET in a cascode form to make a power device that is normally-off, as shown in Fig. 9.

Due to the maturity of the wafer fabricating process, the GaN-on-Si FET has received extensive attention and research. Its typical structure is shown in Fig. 10(a). Like the lateral GaN diode, the lateral GaN FETs utilize high electron mobility in the 2DEG to conduct current. This type of device is called the HEMT. In Fig. 10(a), the 2DEG exists even when the gate-to-source bias voltage is zero, so it is a normally-on depletion transistor. A cascode low-voltage Si-MOSFET can be applied to form a normally-off power device. Despite the cascode form, a true normally-off GaN E-HEMT can be realized by deploying a P-GaN layer between the gate and the AlGaN barrier. By appropriately designing the doping concentration and layer thickness, the P-GaN layer is able to deplete the 2DEG under the gate electrode, making it a normally-off power device [30].

Since the lateral GaN HEMT does not have a junction structure, there is no avalanche phenomenon for lateral GaN devices. The over voltage breakdown for a GaN device will be destructive. In general, the actual breakdown voltage for GaN devices is much higher than the rated voltage. The 650-V GaN devices from Transphorm break down at over 1300 V [49]. The reason for designing such a high breakdown voltage is mainly from the consideration of the dielectric lifetime model.

To fully utilize the GaN material potential, vertical GaN-on-GaN devices are also proposed recently. Fig. 10(b) shows the structure of a normally-off vertical GaN-on-GaN Fin FET studied in 2017. Recently, vertical FETs based on cost-effective GaN-on-Si wafers have also been studied [50]. However, compared with the lateral structure, the ON-resistance of the GaN-on-Si vertical structure does not show many advantages due to the series resistance introduced by the buffer layer [51].

4) Bipolar WBG Power Transistors and Thyristors: Both majority and minority carriers are used by bipolar power devices to conduct current. Conductivity modulation is achieved by injecting minority carriers into the drift region, ensuring a low ON-resistance of the device even at high current density. The switching speed of the bipolar device is slower than the unipolar devices due to the stored charge in the drift region. Due to the high breakdown electric field, the drift region of a WBG bipolar device is much thinner than that of a silicon device. The stored charge in the drift region is one order of magnitude lower than that

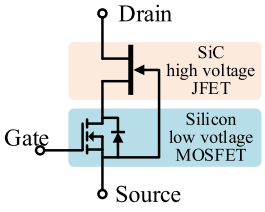

Fig. 9. *Cascode normally-off SiC JFET.*

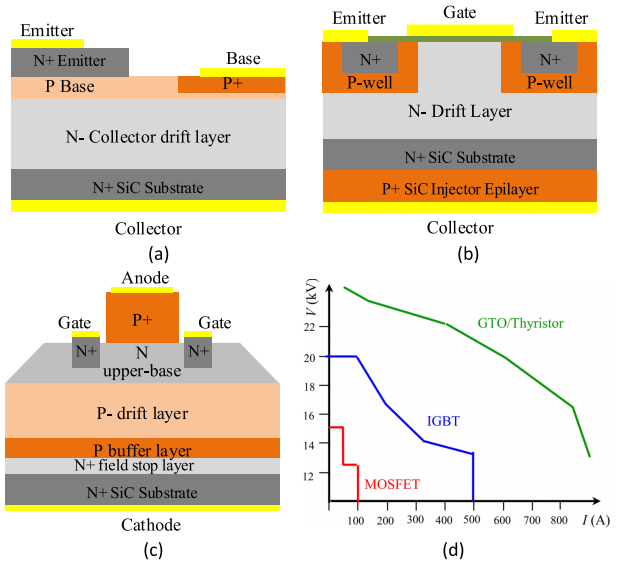

Fig. 11. ***Typical bipolar SiC devices and comparison. (a) SiC BJT [58]. (b) SiC IGBT [59]. (c) SiC GTO [60]. (d) Applicable ratings comparison [61].***

of silicon devices. Furthermore, the lifetime of minority carriers is two orders of magnitude shorter [52]. The switching frequency of WBG bipolar devices is expected to be much higher than the corresponding silicon devices. As a high-voltage and high-power device, most bipolar power devices have a vertical structure. Due to the lack of high-quality, low-cost, free-standing GaN wafers, there is less research on GaN bipolar devices. The most commonly seen bipolar WBG devices are SiC bipolar junction transistor (BJT), SiC IGBT, and SiC GTO. The typical structures of the SiC bipolar devices are shown in Fig. 11. The comparison of applicable voltage and current ratings of SiC MOSFET, SiC IGBT, and SiC GTO/Thyristor is given in Fig. 11(d).

5) Performance of WBG Transistors and Thyristors: Similar to diode performance statistics, R_{onsp} versus V_B is also used to evaluate the performance of WBG transistors and thyristors, as shown in Fig. 12. Research results in 2009 [53] and 2017 [54] show that SiC JFET and MOSFET almost reach the material limit. SiC JFET and MOSFETs have already been on the market for more than ten years. For the performance of GaN-on-Si [55], [56] and GaN-on-GaN [57] FETs, although it is still far from the GaN material limit, it is very close to the SiC material limit. Considering that the cost of GaN-on-Si wafers is much lower compared to SiC, lateral GaN HEMTs have developed rapidly, and commercial devices have also been on the market for a few years.

The theoretical R_{onsp} limit is derived base on the 1-D device model. The superjunction (SJ) structure proposed in the 1990s is a major breakthrough in the field of power semiconductors [62]. A number of thin P- and N-type layers are configured alternatively to form a 2-D structure. Compared with the 1-D structure, the electric field is more uniform, and a thinner drift layer can be used under the same breakdown voltage. Moreover, the doping concentration can be increased. The thinner drift layer and higher doping can reduce the ON-resistance by two orders of magnitude. The theoretical R_{onsp} limit for an SJ structure is given in [62] as

$$R_{\text{onsp}} = \frac{4dV_B}{\mu\varepsilon E_c^2} \tag{2}$$

where d means the thickness of the thin P- and N-layers. Thinner layers can significantly reduce the ON-resistance, but the fabricating process becomes more difficult. The dashed lines in Fig. 12 show the theoretical limit of R_{onsp} for the SJ device when d is 1 μm. The SJ structure promises a further improvement in the performance of the WBG devices. In 2014 and 2018, 1545-V/1.06-m$\Omega \cdot$ cm^2 and 1170-V/0.63-m$\Omega \cdot$ cm^2 SiC SJ MOSFETs were designed and fabricated, respectively [63], [64]. R_{onsp} has already broken through the limit of the SiC 1-D device. The process of GaN material fabrication is more challenging. GaN SJ devices are still in the simulation research phase, and so far, there are no fabricated GaN SJ FETs available [65].

There are already a number of commercial WBG power devices on the market with a voltage rating below 1700 V. The R_{onsp} versus V_B figure is mainly related to the device statics performance. To evaluate the switching dynamic performance, other FOMs, such as $R_{\text{ON}} \cdot Q_g$, and $R_{\text{ON}} \cdot C_{\text{oss}}$, are usually referred to, where R_{ON} is the device ON-resistance, Q_g is the gate charge when switching, and C_{oss} is the output equivalent capacitance. The reverse recovery time t_{rr} and charge Q_{rr} are also associated with switching losses and affect the switching frequency. Table 2 gives a comparison of seven state-of-the-art power devices from different manufactures. All the devices have a maximum blocking voltage of 650 V and

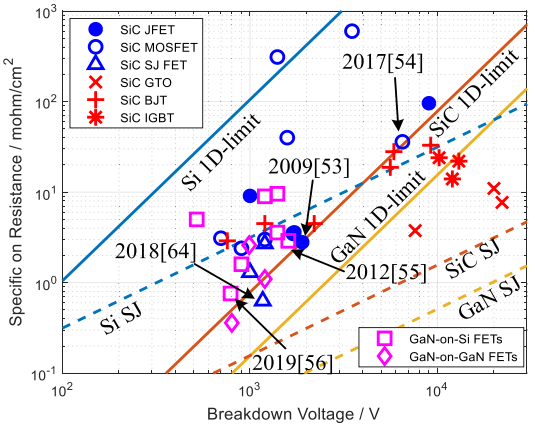

Fig. 12. ***R_{onsp} versus breakdown voltage of WBG transistors and thyristors.***

Table 2 Performance Comparison of Silicon, SiC, and GaN Devices

Model	Manufacture	Device Type	R_{on}(mΩ) Typical	R_{on}·Q_g (mΩ·nC)	R_{on}·C_{oss} (mΩ·pF)	t_{rr}(ns)	Q_{rr}(nC)	R_{on}@125°C*
IPW65R041CFD	Infineon	Si SJ MOSFET	37	11100	14800	250	1900	2.16
SCT3030AL	Rohm	SiC MOSFET	25	2600	2225	26	130	1.6
SCTH100N65G2	ST	SiC MOSFET	20	3240	5340	26	370	1.31
IMZA65R027M1H	Infineon	SiC MOSFET	27	1701	6588	102	239	1.22
UF3C065030B3	UnitedSiC	SiC Cascode JFET	27	1377	7911	34	211	1.3
GS66516T	GaN System	GaN E-HEMT	25	302.5	3250	0	0	2.25
TP65H035WSQA	Transphorm	Cascode GaN HEMT	35	840	6860	65	178	1.75

* Normalized to R_{on} @ 25 °C

similar ON-resistance, and the smaller $R_{ON} \cdot Q_g$, $R_{ON} \cdot C_{oss}$, t_{rr}, and Q_{rr}, the better the high switching characteristics. From Table 2, the silicon SJ MOSFET has the largest $R_{ON} \cdot Q_g$, $R_{ON} \cdot C_{oss}$, t_{rr}, and Q_{rr}, which means that its switching characteristics are the worst. Also, silicon MOSFET has the second highest normalized R_{ON} @ 125 °C. SiC and GaN power devices have exceeded the performance of Si MOSFETs in almost all aspects. The revolution of WBG devices to replace traditional Si MOSFETs is already underway.

D. Driving Issues

For WBG devices in modular form, a dedicated driving circuit is usually provided by the manufacture or a professional third party. Most researchers and engineers will face how to design a driving circuit for discrete WBG devices. Driving WBG devices is similar to driving Si MOSFETs as most WBG devices are voltage-controlled devices. Special attention should be paid to the difference in driving voltage between the WBG device and the silicon device. Usually, the recommended turn-on gate voltage of SiC MOSFETs is higher than Si MOSFETs, while the threshold voltage V_{th} is about the same or even lower compared with Si MOSFETs. To avoid spurious gate turn-on induced by high *di/dt* during the switching actions, a negative turn-off voltage is usually required for SiC devices. Compared with Si MOSFETs, the maximum allowable gate voltage range of SiC is narrower, which means that the safety margin of the gate voltage is narrowed.

The gate voltage safety margin problem of the GaN device is more serious. The gate-ON voltage for GaN E-HEMTs can be only 5–6 V. The low driving voltage significantly reduces the driving power requirement, especially in MHz switching applications. However, the maximum allowable gate voltage of GaN E-HEMT is less than 10 V. For example, the maximum allowable gate dc voltage of GaN Systems 66516T is only 7 V. The gate voltage safety margin of the enhanced mode GaN devices can be as low as 1 V, which is the major challenge for the driving circuit design.

The normally-off cascode device consists of a normally-on depletion WBG device and a low-voltage MOSFET structure. The gate drive characteristics are determined by the low-voltage MOSFET, and its driving requirements are exactly the same as the low-voltage MOSFET. For the cascode structure, standard silicon gate driving techniques can be applied directly. There are two problems brought by the cascode structure. One is the reverse recovery caused by the low-voltage silicon MOSFET, and the other is voltage distribution in the dynamic switching process. It is imperative to match the output capacitance of the high- and low-voltage devices. If the matching is not appropriate, it will cause an avalanche breakdown of the low-voltage device and increase losses [66].

A driving characteristics comparison of different structure power devices is given in Fig. 13. It can be seen that the GaN E-HEMT has the narrowest safety margin against the gate overvoltage breakdown and spurious turn-on. Infineon uses another way to improve the gate ruggedness in their CoolGaN products [67]. A similar gate structure can also be found in Panasonic X-GaN products. A self-clamping p-gate structure is adopted to solve the over voltage sensitivity brought by the reverse Schottky p-gate structure. The drawback is that a special current source driver of a few milliamperes is required, which may slightly increase the driving loss.

E. Reliability Concerns

With the advanced performance of SiC and GaN power semiconductors, more and more power electronics converters are migrating from silicon to WBG. Due to the

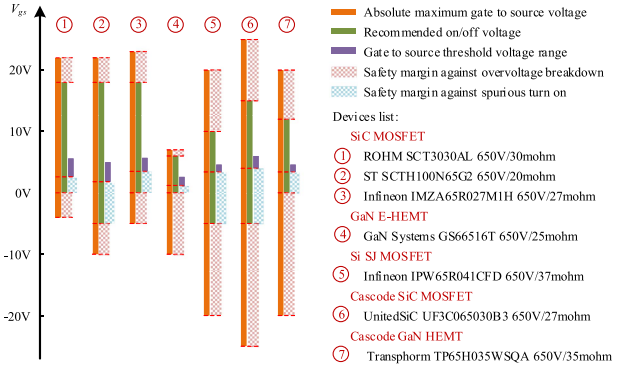

Fig. 13. ***Comparison of gate driving voltage and safety margin.***

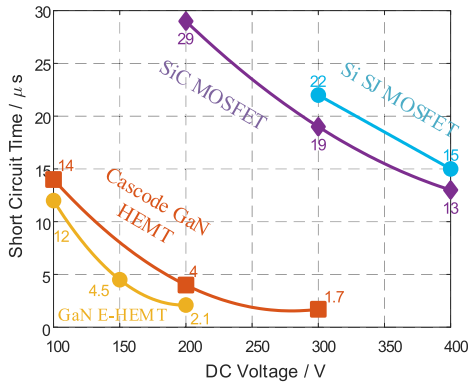

Fig. 14. ***Short-circuit endurance comparison [72].***

ruggedness of WBG devices in terms of temperature, breakdown voltage, and avalanche energy, in most cases, WBG devices can take the place of Si devices when a proper driving circuit is designed. Various research works have also been conducted to ensure the reliability of WBG devices.

1) SiC Diode Reliability: Infineon studied the reliability of SiC MPS diodes through various tests in 2006 [68]. The diode can withstand continuous avalanche power dissipation of 20 W/mm^2 for 1000 h. The switching *dv/dt* ruggedness was also tested under 90 V/ns for more than 3.6×10^{11} cycles at 150 °C. In addition, the current stress test was carried out for 1 h under the condition of current density as high as 4.6 kA/cm^2, which is equivalent to 3.6×10^5 times of 10-ms half-sine wave surge current. After all the extreme stress tests, the diode has no noticeable degradation, showing a large margin of reliability when using SiC diodes under normal conditions.

2) Gate Reliability: The gate reliability of SiC MOSFET is usually considered to be more robust than GaN E-HEMT devices due to higher safety margins. Besides the gate voltage breakdown safety margin, attention should be paid to the gate deterioration of WBG devices due to long-term or repeated fatigue. One finding is that the repetitive short circuit will degrade the gate of the SiC MOSFET, which is manifested as an increase in the leakage current and change in threshold voltage and input capacitance, while the same problem does not occur in Si MOSFETs [69], [70]. The causes of the gate failure under short-circuit stress have been studied, and some possible solutions are suggested in [71].

3) Short-Circuit Endurance: The short-circuit characteristics are related to equipment fault tolerance and the design of protection, which is critical to the reliability of the converter [73]–[75]. The short-circuit withstand time of four different types of devices on the market, Silicon SJ MOSFET, SiC MOSFET, Cascode GaN HEMT, and GaN E-HEMT, is tested and given [72], as shown in Fig. 14. The SiC MOSFET has a similar withstand time compared with Si SJ MOSFET. For GaN HEMT, its withstanding time is much shorter, which indicates that the GaN HEMT device has the worst short-circuit endurance among the tested devices.

4) Long-Term Reliability: Industrial manufacturers and academic researchers have conducted various studies on the long-term reliability and lifetime estimation of WBG devices. Wolfspeed's research shows that the reliability and lifetime of SiC MOSFETs are generally similar to Si IGBT devices. The failures per billion device hours (FIT) of SiC MOSFETs are even lower than those of Si IGBT devices. The expected average lifetime of 1200-V/80-mΩ SiC MOSFETs at 800-V dc voltage exceeds 3×10^7 h [76]. Efficient power conversion (EPC) studied the reliability of their low-voltage GaN devices. Based on data obtained from six years and 17 billion hours of operation, an FIT rate of 0.24 of low-voltage (100 V) GaN devices is calculated, which is even better than silicon MOSFETs [77]. GaN device manufacture Transphorm also studied the reliability of its cascode GaN devices using existing industrial and automotive standards [49]. The results show that their 650-V/62-mΩ GaN cascode HEMT meets the automotive-grade AQ101 standard. The manufactures' reliability data are derived mainly from experimental data. The failure mechanism and lifetime prediction model of SiC and GaN devices and converters have also been extensively studied by academia [70], [78]–[81]. WBG device lifetime under high temperature is also studied. The SiC MOSFET is expected to have a lifetime of 100 years at 375 °C with an operation electric field strength of 3.9 MV/cm [82]. With an in-depth understanding of the failure mechanism, the reliability of WBG-based converters is expected to exceed traditional Si-based converters, especially under a high-temperature environment. WBG devices are expected to be more reliable than traditional silicon devices, which is preferable for both EV OBC and off-board fast-charging station applications.

III. ONBOARD CHARGER APPLICATIONS

A. Topology Evolution

The OBC can be realized as the nonintegrated OBCs or the integrated OBCs [83]. The nonintegrated OBC is a separate charging circuit, which only serves as the propulsion battery charger. The integrated OBC reuses the existing components of the inverter and the electric motor for the propulsion battery charging circuit, so the cost and weight of the OBCs can be reduced [84]. For the nonintegrated OBC, it can be realized as the single- or three-phase topologies. The single-phase topology is usually used for low-power OBCs, where the charging power is less than 10 kW [2], [83], [85]. The traditional structure of a single-phase OBC is shown in Fig. 15 [86]. A diode-based rectifier and an active front-end PFC converter are used to interface to the ac grid. The output of the PFC is followed

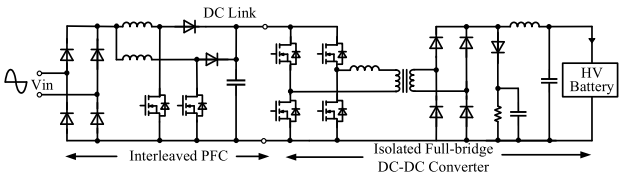

Fig. 15. *Typical structure of the single-phase OBC topologies.*

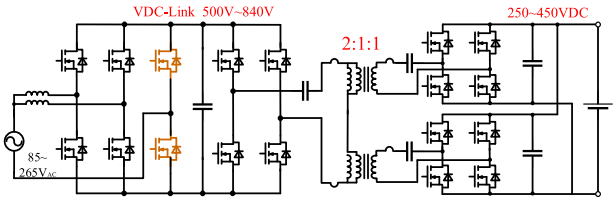

Fig. 17. *Single-phase OBC based on a two-phase interleaved totem-pole PFC and a CLLC resonant converter.*

by an isolated dc–dc converter, which is connected to the propulsion battery.

To reduce the conduction loss of low-frequency rectifier, a boost bridgeless PFC can be adopted by directly connecting the ac grid with two boost converters [87], as shown in Fig. 16(a). In order to reduce the common-mode noise, two additional diodes are required to provide a current return path [88].

By exchanging the position of a diode and a MOSFET, the totem-pole bridgeless PFC can be implemented, as shown in Fig. 16(b). In the totem-pole structure, the two diodes can be slow reverse recovery diodes, providing lower ON-voltage compared with the two fast diodes in the two-boost bridgeless PFC, which is essential for high efficiency. However, due to the poor reverse recovery of silicon MOSFETs, totem-pole PFC was once considered impractical [88]. Due to the excellent reverse recovery performance of the WBG device, the high-efficiency totem-pole bridgeless PFC rectifier can be adopted in the ac–dc stage. A 99% peak efficiency totem-pole continuous conduction mode (CCM) PFC with GaN HEMT was reported by Transphorm in 2015 [89]. A higher power density can also be realized at MHz switching frequency with the zero-voltage switching (ZVS) method [90]. In 2017, a two-phase interleaved totem-pole critical mode (CRM) GaN-based PFC is used as the rectifier stage, followed by a *CLLC* resonant converter as the dc/dc stage [85], as shown in Fig. 17. A variable dc bus voltage of 500–840 V is adopted, and a bidirectional 6.6-kW OBC with efficiency above 96% is realized.

When the power of OBC is greater than 10 kW, the three-phase ac input is usually adopted, and the common structure is the three-phase full-bridge topology. By simply replacing Si IGBT with SiC MOSFET, the efficiency and power density of the three-phase rectifier can be significantly improved due to lower conduction loss and higher switching frequency [91].

In [92], a three-phase 10.5-kW OBC is proposed with three single-phase modules similar to Fig. 15. By changing the wiring configuration, single- and three-phase input compatibilities can be achieved. A single-stage, bidirectional dual-active-bridge (DAB) converter is adopted as the single-phase ac–dc module to increase the efficiency and power density [11], as shown in Fig. 18. Three single-phase modules form a three-phase OBC, which can provide 22-kW power to the propulsion battery. GaN E-HEMT devices are adopted as the main switches. The input four switches work in low-frequency synchronous rectification mode, and the power factor and power output are all controlled by the dc–dc stage. The ac input power is directly transferred to the battery, so the dc bus capacitance can be greatly reduced, and high-power density can be achieved.

B. Efficiency and Power Density With WBG Devices

The efficiency comparison of the commercially available Si-based OBCs and laboratory SiC-based OBC prototypes is shown in Fig. 19 [11], [83], [85], [87], [93], [94].

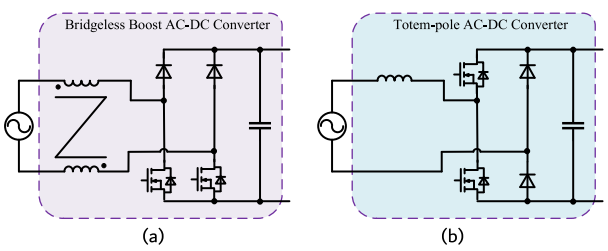

Fig. 16. *Bridgeless ac–dc converters. (a) Two boosts. (b) Totem-pole.*

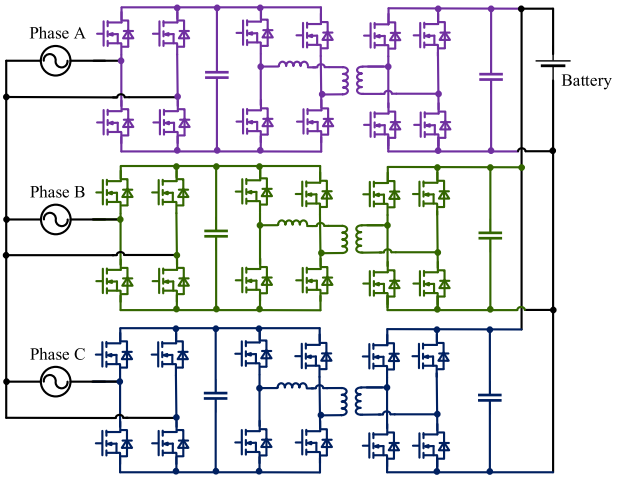

Fig. 18. *Three-phase OBC based on three paralleled single-stage single-phase OBCs [11].*

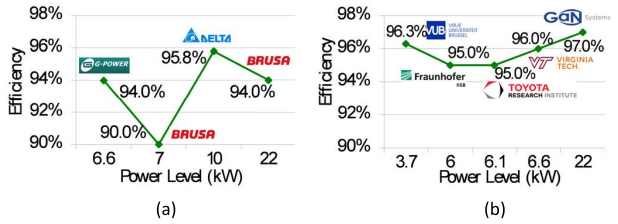

Fig. 19. *Efficiency comparison. (a) Commercial OBCs. (b) WBG-based OBC prototypes.*

The efficiency of SiC-based OBCs has obvious advantages over Si-based OBCs. The highest efficiency reaches 97% by using GaN power devices [11]. Fig. 20 gives the power density comparison. The power density of commercially available OBC is less than 2 kW/L. The highest power density of SiC-based OBC reaches 5 kW/L, which is twice that of Si-based OBC. In 2018, Level-2 integrated OBCs based on Si, SiC, or GaN power devices are investigated, and a comparison of weight, volume, and peak efficiency for the isolation converters is presented [8]. Compared with the Si-based isolation converter, the SiC-based isolation converter can increase 72% in power density and 81% in specific power. By using GaN-based power devices, an increase of 170% in power density and 500% in specific power can be achieved. In [95], it is demonstrated that SiC-based OBC solution can achieve a 60% weight and volume reduction compared with the Si-based solution. For the WBG device-based OBCs, the GaN HEMT-based OBC is supposed to be smaller and more efficient, while the SiC MOSFET-based OBC exhibits a better thermal performance [96].

IV. FAST-CHARGING STATION APPLICATIONS

A. Topologies Evolution

The traditional fast-charging station is based on a low-frequency transformer, as shown in Fig. 21. It can be realized as the common ac bus architecture or the common dc bus architecture. For the ac bus architecture, each charger consists of a separate ac–dc converter and a dc–dc converter. For the dc bus architecture, the common dc bus is created by a central front-end ac–dc converter.

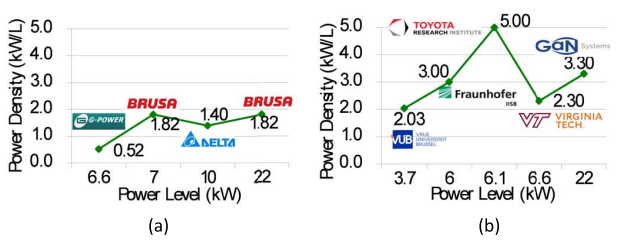

Fig. 20. *Power density comparison. (a) Commercial OBCs. (b) WBG-based OBC prototypes.*

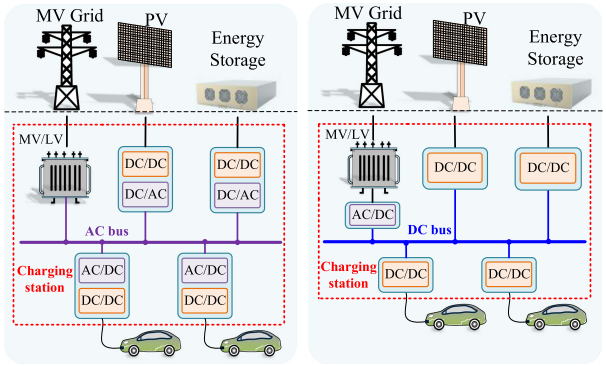

Fig. 21. *Architectures of traditional fast-charging stations [5]. (a) Common ac bus architecture. (b) Common dc bus architecture.*

Each charger consists of a dc–dc converter and is directly connected to the common dc bus. The common dc bus architecture is preferred because fewer conversion stages are needed between the common bus and the EV or the renewable energy sources, which can reduce the system complexity, cost, and power loss [97]. The common dc bus can be built as a unipolar dc bus [98] or bipolar dc bus [99]. Currently, unipolar dc bus topology is widely used in the commercially available dc fast chargers because of the simple structure, well-established control schemes, and low cost [97]. Fig. 22 shows the bipolar dc bus using three-level DNPC, and a two-phase three-level buck converter is used as the charger [99]. More power capacity can be offered by using the bipolar dc bus, and there are more flexible ways to connect the loads to the dc bus.

The fast-charging station can also be built by MV directly connected fast-charging topologies, which is also mentioned as an SST-based fast charger. In the SST-based fast charger, the low-frequency transformer is replaced by a high-frequency transformer. The active front-end converter directly interfaces to the MV grid, followed by high isolation dc–dc converters, as shown in Fig. 23. The low-voltage dc bus is obtained from the isolated dc–dc converters. One or more isolated or nonisolated dc–dc converters

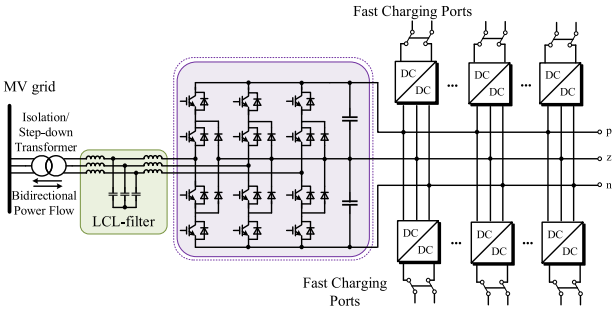

Fig. 22. *Bipolar dc-bus using three-level DNPC and a two-phase three-level buck converter as the charger [99].*

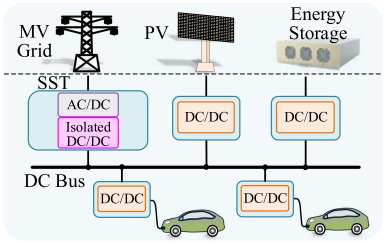

Fig. 23. *Modular SST-based fast charger using cascaded three-level DNPC-bridge converters and LLC converters.*

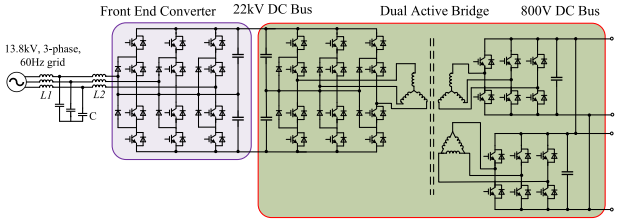

Fig. 25. *Three-phase single-module SST-based fast charger based on three-level converters [107].*

are connected to this dc bus as the charger [100]. The SST-based fast charger can be realized as the modular SST-based or single-module SST-based architectures. For the modular SST-based architecture, the multilevel converter, such as cascaded H-bridge converter, is usually employed as the active front-end converter [101], [102]. The output of each H-bridge is followed by an isolated dc–dc converter. The H-bridge can also be replaced by the three-level DNPC-bridge, as shown in Fig. 24. The advantages of using the three-level DNPC-bridge include fewer isolation components, simple structure, lower cost, better THD, smaller filter, and higher efficiency [100]. In Fig. 24, each DNPC-bridge is followed by an *LLC* resonant dc–dc converter to create a 1-kV dc bus. Then, interleaved buck converters are connected to this dc bus to regulate the charging power. The 1200-V/1700-V SiC MOSFETs are adopted to improve system efficiency. In [103], a 25-kW all-SiC MVAC-LVDC SST based on direct ac–ac isolated front-end converter is proposed. The output of the isolated front-end converter is the rectified low voltage, which is the absolute value of the ac voltage on the secondary side. A boost PFC is followed to convert this ac voltage to a constant dc voltage. The power density of 1.5 kW/L and the modular efficiency of 97.5% are achieved with this topology.

The number of active switches can be reduced by adopting uncontrolled diode bridge rectifiers [104], [105]. Consequently, the system cost can be reduced. However, these topologies can only provide unidirectional power flow with limited reactive power control. Moreover, when using a diode rectifier, one more power device will be in the main current path compared with all active switches, which lowers the highest possible efficiency.

In an SST-based modular fast charger, commercialized WBG devices with a voltage rating of 1200 V/1700 V can be used. However, as the MV grid voltage usually ranges from 2.4 to 13.8 kV, dozens of modules are needed to adapt the high voltage for a three-phase system, resulting in complicated topology and multiple control loops. With the development of 10 kV or above voltage rating SiC-MOSFET and SiC-IGBT, the single-module SST-based fast charger can be employed. A single two- or three-level converter is used to directly connect to the MV grid, which can significantly reduce the complexity of the system. In 2014, a single-phase 10-kW SST is directly connected to a 3.6-kV MV grid based on 13-kV SiC MOSFETs and JBS diodes [106]. In 2015, a three-level DNPC with 15-kV SiC IGBTs and 10-kV SiC MOSFETs is adopted to directly interface a 13.8-kV MV grid [107], as shown in Fig. 25. For the isolation stage, a three-phase DAB is selected with a three-level DNPC-bridge on the primary side and a two-level bridge on the secondary side. The internal dc bus voltage is 22 kV, and its output dc voltage is 800 V. In 2019, another single-phase 25-kW SST is realized based on 10-kV SiC MOSFETs [108], [109]. The input ac voltage is 3.8 kV, and the intermedia dc bus voltage is 7 kV. For the isolation stage, an *LLC* resonant converter is selected with a half-bridge on the primary side and an H-bridge on the secondary side. The efficiency at full load for the complete SST system achieved 98.1%. The single-module SST-based fast charger not only has simple topology and control but also shows higher power density and efficiency compared with the modular SST-based fast charger.

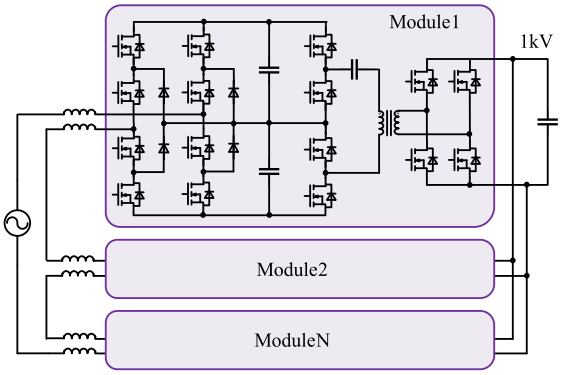

Fig. 24. *Modular SST-based fast charger using cascaded three-level DNPC-bridge converters and LLC converters.*

B. Efficiency and Power Density With WBG Devices

The efficiency of the commercially available dc fast chargers is around 93% (92%–95%), as shown in Fig. 26(a) [5]. If the efficiency of the distribution transformer is taken into consideration [110], the overall efficiency would be further reduced by 0.5%–1%. The efficiency of SST-based dc fast chargers is around

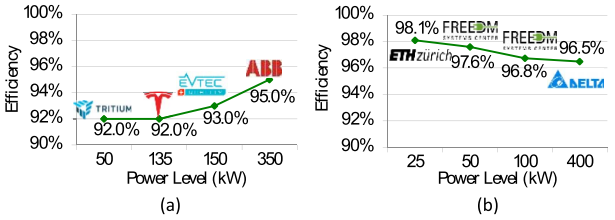

Fig. 26. *Efficiency of dc fast chargers. (a) Commercially available dc fast chargers [5]. (b) SST-based dc fast chargers.*

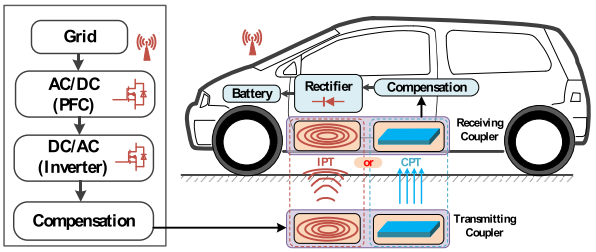

Fig. 28. *Structure of a typical EV wireless charging system.*

97% [5], [100], [107]–[109], as shown in Fig. 26(b). Since the low-frequency transformer is eliminated in SST-based dc fast chargers, the overall efficiency can be improved by 2%–3% compared with the existing transformer and charger system.

The power density of the commercially available dc fast chargers is below 200 W/L, as shown in Fig. 27(a). Currently, there are no commercialized SST-based dc fast chargers. The power density of the SST prototype can achieve 0.403 and 0.81 kW/L by using 1200-V/1700-V SiC MOSFETS, as shown in Fig. 27(b). The power density can be further improved to 1.761 kW/L by using 10-kV SiC MOSFETS. When replacing the existing transformer and fast charger system with an SST-based dc fast charger, the volume can be reduced by 30 times and saving more than half of the cost at the system level [5].

V. WIRELESS CHARGING APPLICATIONS

A. Introduction to Wireless Charging

Wireless charging, which uses an inductive or capacitive coupled method to transfer electric power without direct contact, is a promising alternative for EV charging against traditional conductive charging [111], [112]. Since there are no charging plugs and cables, wireless charging is safer, more convenient, and reliable. The structure of a typical EV wireless charging system is shown in Fig. 28. The power is transferred from the grid to the battery through a high-frequency magnetic or electric field.

In recent years, extensive studies have been carried out on IPT and CPT, and many wireless charging prototypes for EVs have been released by companies, such as WiTricity, Qualcomm Halo (acquired by WiTricity in 2019), Plugless Power, OLEV, Bombardier Primove, Momentum Dynamics, and Conductix-Wampfler [113]. The power and efficiency of these prototypes are given in Table 3. The wireless chargers have achieved similar or even higher power than the OBC. The efficiency of 90% or higher can also be achieved, which is very attractive considering the safety and convenience brought by wireless charging.

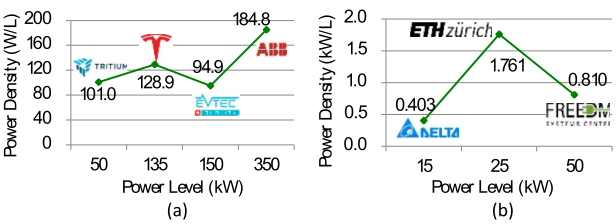

Fig. 27. *Power density of dc fast chargers. (a) Commercially available dc fast chargers [5]. (b) SST-based dc fast chargers (power modular).*

B. Research Progress

The research papers related to WPT from the years 2000 to 2019 are collected and summarized using Google Scholar. The total number of papers and the number of papers indicating the use of WBG devices are shown in Fig. 29. The number of papers related to WPT has increased rapidly since 2007; in that year, the Massachusetts Institute of Technology (MIT) demonstrated their 2-m 60-W wireless power transfer (WPT) system [114]. WBG devices have shown great advantages in high-speed switching. Since 2010, the number and ratio of WPT research papers that clearly stated the use of WBG devices have increased rapidly.

For the inductive-coupled WPT, the key elements of the WPT system, such as coil structure [115], [116], compensation topology [117], [118], and control methodology [119], [120], have been widely studied. The reported IPT systems transfer power up to 100 kW at an airgap of 10 to 300 mm, together with an efficiency of 70%–98% at the operating frequency of 10 kHz–13.56 MHz [121]–[124].

The maximum transfer power and dc-to-dc efficiency of an inductive-coupled WPT system can be calculated using (3) and (4) [125]. ω is the system angular frequency;

Table 3 Specifications of EV Wireless Charging Prototypes

Company	Power	Frequency	Airgap	Efficiency
Plugless power	3.6 – 7.2 kW	N/A	100 mm	90%
WiTricity	11 kW	85 kHz	100-250 mm	90-93%
Qualcomm Halo	Up to 20 kW	85 kHz	160-220mm	90%
HEVO Power	2-10 kW	85 kHz	304.8mm	85%
Conductix Wampfler	60-180 kW	20 kHz	40 mm	> 90%
Momentum Dynamics	10 kW	20 kHz	200 mm	>92%
Bombardier	200 kW	N/A	10-30 mm	>85%

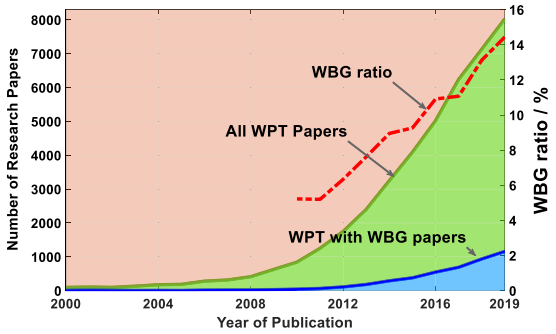

Fig. 29. ***Research paper number and ratio.***

M is the mutual inductance between the transmitting and receiving coils. I_1 and I_2 are the currents in transmitting and receiving coils, respectively. It is clear that, with the same mutual inductance and current configuration, the transferred power is proportional to frequency. Q_1 and Q_2 are the quality factors of the transmitting and receiving coils; k is the coupling coefficient between the transmitting and receiving coils, as defined in (5). L_1 and L_2 are the inductances of the two coils, while R_1 and R_2 are the coil resistances at the operating frequency. When appropriate Litz wire is adopted, increasing the frequency can improve the coil quality factor, and the maximum efficiency will also increase

$$P = \omega M I_1 I_2 \tag{3}$$

$$\eta_{\max} = \frac{k^2 Q_1 Q_2}{\left(1+\sqrt{1+k^2 Q_1 Q_2}\right)^2} \tag{4}$$

$$Q_1 = \omega L_1/R_1, \quad Q_2 = \omega L_2/R_2, \; k = M/\sqrt{L_1 L_2}. \tag{5}$$

Although the SAE J2954 standard specifies the operating frequency around 85 kHz (81.38–90 kHz), higher frequency shows superior characteristics in terms of efficiency and power density. The study from ETH Zürich also shows that high power density and efficiency can be realized by increasing the frequency properly [116]. Compared with Si devices, the switching frequency of WBG devices can be up to MHz, providing a better choice for wireless charging applications.

The dual of inductive-coupled WPT is the capacitive coupled WPT. For many years, the CPT system can only transfer low power over a short distance. Usually, the power is limited to a few watts [126], and the distance is less than 10 mm [127], [128]. With the development of WBG power devices and compensation topology [129], the CPT system can transfer kilowatt power at MHz, together with an efficiency over 90% [130], and the airgap can also be as large as 150 mm [131]–[133], showing the great potential of CPT in EV wireless charging applications [134].

To compare the performance difference of Si, SiC, or GaN devices in WPT, the latest research papers on WPT applications with power higher than 100 W are collected and summarized. Fig. 30 shows the comparison of the power and efficiency of the WPT system. All three types of devices can reach a dc-to-dc efficiency higher than 95% [121], [123], [135]. Si and SiC devices are mostly used in applications with power up to tens of kilowatts, while GaN devices are mainly used for devices with power below 2 kW. When the transferred power is higher than 10 kW, SiC devices perform better than Si devices in terms of efficiency.

C. Figure of Merit for WPT Systems

The performance of the WPT system can be evaluated from its transferred power P, dc-to-dc efficiency η, air gap d, and coupler area S. When the transmitting and receiving coupler areas are different, the geometric mean of the two areas can be used as the coupler area S. Higher power, efficiency, and air gap are always desired with a smaller coupler area. Thus, a WPTFOM can be designed as follows:

$$\text{WPTFOM} = \frac{P \cdot d}{(100 - \eta \cdot 100) \cdot S^{3/2}}. \tag{6}$$

The 3/2 order of the coupler size S comes from two parts. First, the power should be normalized to the unit coupler area S to represent the power density. The remaining 1/2 order is related to the coupling coefficient. For a given shape of the coil, the coupling coefficient is proportional to $\sqrt{S}/d$ [136]. We would like to optimize the coil structure for a higher coupling coefficient with a smaller size and a larger airgap. Thus, the coupling coefficient related to the size and airgap parameters should be normalized. Similar coupling coefficient ideas can also be applied to CPT couplers; thus, (6) is also applicable for CPT systems [137]. It can be seen that the WPTFOM has a unit of W/m^2. The proposed WPTFOM can represent the power density of a WPT system while considering efficiency and transfer air gap at the same time.

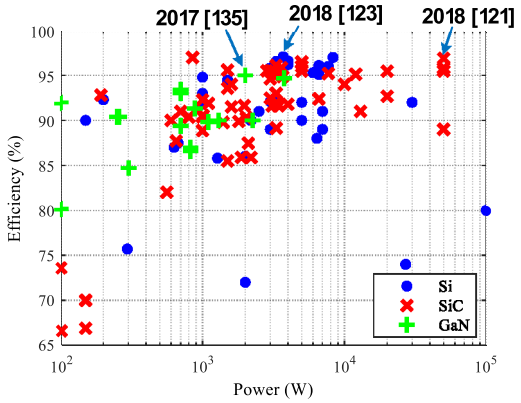

Fig. 30. ***Efficiency versus output power.***

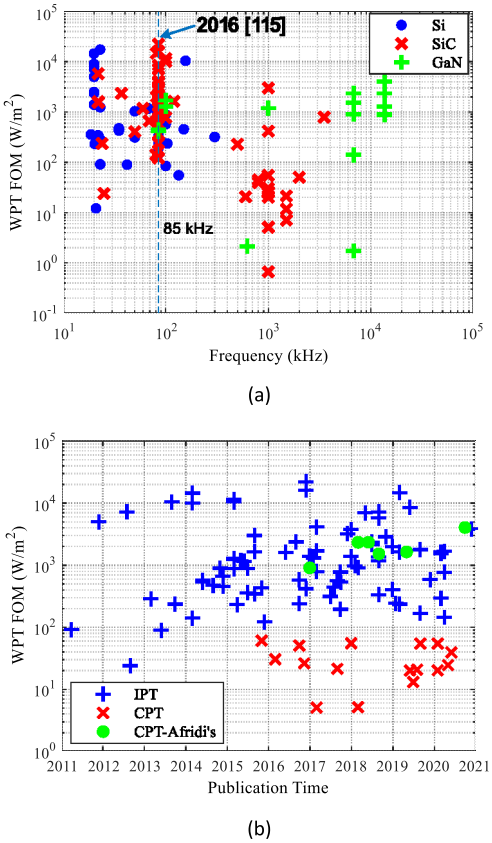

Fig. 31. *Comparison of WPTFOM (a) versus frequency for Si, SiC, and GaN devices and (b) versus time for IPT and CPT in EV WPT applications.*

Fig. 31(a) shows the relationship between WPTFOM and frequency for the wireless charger using Si, SiC, and GaN devices. The system based on SiC has obvious advantages when evaluated by WPTFOM. The highest WPTFOM is achieved at a frequency of 85 kHz with SiC devices [115]. One possible reason is that the frequency recommended by the WPT standards is around 85 kHz; most IPT system is studied and optimized at this frequency. At higher frequencies such as around 1 MHz, the researchers focus more on the CPT system, and currently, the WPTFOM of a CPT system is much lower than that of an IPT system.

For EV wireless charging, in addition to considering the area of the coupler, we also prefer a thinner and lighter coupler at the EV side. A modified WPTFOM by multiplying a factor of $1/h$, where h is the thickness of the receiving coupler, could be more comprehensive. However, there is very limited data published about the coupler thickness. In this case, we still use WPTFOM defined in (6) to evaluate the state-of-the-art EV WPT system published in recent ten years, as shown in Fig. 31(b). It can be seen that, for EV wireless charging, the IPT system has a much higher WPTFOM than that of CPT systems. Khurram K. Afridi's recent research on high-frequency (6.78 and 13.56 MHz) CPT systems has shown great advances in CPT systems [138]–[143]. WPTFOMs of these CPT systems are already comparable to IPT systems. However, there are two points that need to be clarified. One is that the efficiency data are from dc-to-ac in most of these studies in [138]–[143]. If dc-to-dc efficiency is adopted, the WPTFOM could be lower. The other point is that there is no information on how the power and efficiency are measured in the experiments. It is difficult to accurately measure high-frequency ac power.

VI. FUTURE TRENDS OF EV CHARGING TECHNOLOGY

A. WBG Devices' Adoption

The SiC Schottky diode below 1700-V ratings is replacing Si fast recovery diode in EV charging applications due to better cost-performance. SiC MOSFETs and cascode normally-off SiC JFET under 1700 V have already been commercialized. SiC FETs currently show a strong advantage at a 1200-V voltage rating. The cost of those SiC devices will be only 1.5 times traditional Si devices when migrating to 200-mm SiC wafers in one or two years. By then, considering the cost reduction of passive components and heat sinks, the total cost of SiC chargers with higher efficiency and power density will be equal to or even lower than Si-based chargers.

Both the GaN-on-Si lateral Schottky and GaN-on-GaN vertical Schottky diodes have surpassed the theoretical limits of the SiC Schottky limit. Considering that the cost of GaN-on-Si wafer is only 1/5 of SiC wafer, GaN-on-Si lateral Schottky would be a potential future diode structure on the market. The performance of GaN-on-Si lateral HEMT has also been very close to the limit of SiC 1-D. Moreover, GaN HEMT is a zero reverse recovery device. For high switching frequency applications with rated voltages below 900 V, GaN HEMTs are also a good choice.

The performances of SiC and GaN devices have already been far beyond the 1-D Si devices limit and superior to the Si SJ MOSFET. The reliability of commercial WBG devices has been verified by mass experiments. The overall converter cost using WBG devices is going to be similar to or even lower than Si devices. It is recommended that SiC or GaN devices should be adopted in all newly designed and developed EV chargers where 1700 V or under-rated voltage devices are needed.

B. Onboard Chargers

WBG devices can achieve higher switching frequency while keeping high efficiency [8]. They will penetrate the high-power OBCs with a higher power density and higher efficiency. For the two-stage OBCs, the totem-pole bridgeless PFC rectifier becomes a popular implementation as the ac–dc stage because of the greatly improved reverse-recovery effect of the WBG-based power devices [85], [144]. Meanwhile, planar magnetics and windings are utilized in order to achieve a higher power density. Moreover, single-stage OBCs based on WBG devices show the advantage to achieve higher efficiency compared with two-stage solutions [11].

C. DC Fast Chargers

SST-based fast chargers directly connected to the MV grid show the advantages in the system-level efficiency, power density, and cost. The SST-based architecture is a trend for the next-generation dc fast chargers. However, there are some challenges to overcome before we can fully exploit the advantages of SST-based technology. The first one is that 10-kV-level SiC MOSFETS and SiC IGBTs are still under development and have not been commercialized; the modular SST-based architecture would be the first choice for the coming MV interfaced dc fast charger. However, the design and control for this modular SST-based dc fast charger are the challenges. The second challenge is the lack of comprehensive and fast-acting protection for MV power converters. The traditional mechanical MV circuit breakers are too slow to protect the MV power converters against the fault currents [5]. The third challenge is the standardization and certification for the SST-based fast-charging equipment. SST-based fast-charging equipment should meet the standard requirements for the MV equipment and the EV chargers developed by IEEE, IEC, CHAdeMo, and SAE [97].

D. Wireless Chargers

When we take efficiency, power, coupler size, and charging distance into comprehensive consideration, WBG-based WPT systems have obvious advantages over silicon-based systems. It is foreseeable that GaN and SiC devices will be the most widely used devices in wireless charging systems. The current wireless charging system achieves the best WPTFOM at 85 kHz, which accords with the latest wireless charging standards. With the continuous improvement of WBG device performance and the development of soft-switching control technology, it is possible to find a much better operating frequency other than 85 kHz for EV wireless charging. Whether it is IPT or CPT, to realize the full potential of WPT technology, we should not limit the frequency of EV wireless charging research and exploration to 85 kHz.

VII. CONCLUSION

WBG devices can greatly improve the performance of EV charging systems from two aspects. One is from the device itself; by directly replacing Si devices with WBG devices, efficiency and power density improvement could be expected. The other is from the topology aspect. Due to the superior performance, especially the fast or zero reverse recovery characteristics, higher efficiency topologies, such as the totem-pole PFC, could be adopted. Fast-charging stations directly connected to the MV power grid also benefit from the increase in the breakdown voltage and the reduction in conduction and switching losses. For EV wireless charging, the current standards set the working frequency around 85 kHz, which is far below the optimal switching frequency of WBG devices. As the size and weight of the WPT coupler are inversely proportional to the operating frequency, a higher frequency for EV wireless charging may also be studied. With the maturity of the wafer process and mass production of WBG power devices, the cost of WBG devices will decrease continuously. The charging equipment with WBG devices is superior to the Si-based equipment from all aspects, including cost. Most of the newly developed EV charging equipment should be WBG devices powered. The era of WBG has arrived. ■

REFERENCES

[1] T. Franke and J. F. Krems, "What drives range preferences in electric vehicle users?" *Transp. Policy*, vol. 30, pp. 56–62, Nov. 2013.

[2] M. Yilmaz and P. T. Krein, "Review of battery charger topologies, charging power levels, and infrastructure for plug-in electric and hybrid vehicles," *IEEE Trans. Power Electron.*, vol. 28, no. 5, pp. 2151–2169, May 2013.

[3] *Chevrolet Bolt EV Specifications*. Accessed: Jul. 31, 2020. [Online]. Available: https://www.chevrolet.com/electric/bolt-ev

[4] *Tesla Model 3 and Model S Specifications*. Accessed: Jul. 31, 2020. [Online]. Available: https://www.tesla.com

[5] S. Srdic and S. Lukic, "Toward extreme fast charging: Challenges and opportunities in directly connecting to medium-voltage line," *IEEE Electrific. Mag.*, vol. 7, no. 1, pp. 22–31, Mar. 2019.

[6] Y. D. Ko and Y. J. Jang, "The optimal system design of the online electric vehicle utilizing wireless power transmission technology," *IEEE Trans. Intell. Transp. Syst.*, vol. 14, no. 3, pp. 1255–1265, Sep. 2013.

[7] *Global EV Outlook 2020*, Int. Energy Agency, Paris, France, 2020.

[8] G.-J. Su, "Comparison of Si, SiC, and GaN based isolation converters for onboard charger applications," in *Proc. IEEE Energy Convers. Congr. Expo. (ECCE)*, Portland, OR, USA, Sep. 2018, pp. 1233–1239.

[9] A. Q. Huang, "Power semiconductor devices for smart grid and renewable energy systems," *Proc. IEEE*, vol. 105, no. 11, pp. 2019–2047, Nov. 2017.

[10] A. K. Agarwal, J. B. Casady, L. B. Rowland, W. F. Valek, M. H. White, and C. D. Brandt, "1.1 kV 4H-SiC power UMOSFETs," *IEEE Electron Device Lett.*, vol. 18, no. 12, pp. 586–588, Dec. 1997.

[11] J. Lu *et al.*, "A modular-designed three-phase high-efficiency high-power-density EV battery charger using dual/triple-phase-shift control," *IEEE Trans. Power Electron.*, vol. 33, no. 9, pp. 8091–8100, Sep. 2018.

[12] B. J. Baliga, *Wide Bandgap Semiconductor Power Devices: Materials, Physics, Design and Applications*. Sawston, U.K.: Woodhead Publishing, 2019.

[13] E. Johnson, "Physical limitations on frequency and power parameters of transistors," in *Proc. IRE Int. Conv. Rec.*, New York, NY, USA, vol. 13, Mar. 1965, pp. 27–34.

[14] B. J. Baliga, "Semiconductors for high-voltage, vertical channel field-effect transistors," *J. Appl. Phys.*, vol. 53, no. 3, pp. 1759–1764, Mar. 1982.

[15] A. Q. Huang, "New unipolar switching power device figures of merit," *IEEE Electron Device Lett.*, vol. 25, no. 5, pp. 298–301, May 2004.

[16] M. Bhatnagar and B. J. Baliga, "Comparison of 6H-SiC, 3C-SiC, and Si for power devices," *IEEE Trans. Electron Devices*, vol. 40, no. 3, pp. 645–655, Mar. 1993.

[17] J. L. Hudgins, G. S. Simin, E. Santi, and M. A. Khan, "An assessment of wide bandgap semiconductors for power devices," *IEEE Trans. Power Electron.*, vol. 18, no. 3, pp. 907–914, May 2003.

[18] A. Elasser and T. P. Chow, "Silicon carbide benefits and advantages for power electronics circuits and systems," *Proc. IEEE*, vol. 90, no. 6, pp. 969–986, Jun. 2002.

[19] S. G. Müller *et al.*, "The status of SiC bulk growth from an industrial point of view," *J. Cryst. Growth*, vol. 211, nos. 1–4, pp. 325–332, Apr. 2000.

[20] M. Treu, R. Rupp, P. Blaschitz, and J. Hilsenbeck, "Commercial SiC device processing: Status and requirements with respect to SiC based power devices," *Superlattices Microstruct.*, vol. 40, nos. 4–6, pp. 380–387, Oct. 2006.

[21] *Why Choose Wolfspeed?* Accessed: Jul. 31, 2020. [Online]. Available: https://www.wolfspeed.com/why-wolfspeed

[22] *Silicon Carbide (SiC) Substrates for Power Electronics | II–VI Incorporated*. Accessed: Jul. 31, 2020. [Online]. Available: https://www.ii-vi.com/product/sic-substrates/

[23] V. Veliadis, "Accelerating commercialization of wide-bandgap power electronics [expert view]," *IEEE Power Electron. Mag.*, vol. 5, no. 4, pp. 63–65, Dec. 2018.

[24] S. T. Kim, Y. J. Lee, D. C. Moon, C. H. Hong, and T. K. Yoo, "Preparation and properties of free-standing HVPE grown GaN substrates," *J. Cryst. Growth*, vol. 194, no. 1, pp. 37–42, Nov. 1998.

[25] A. Wakahara *et al.*, "Hydride vapor phase epitaxy of GaN on $NdGaO_3$ substrate and realization of freestanding GaN wafers with 2-inch scale," *Jpn. J. Appl. Phys.*, vol. 39, no. 4S, p. 2399, Apr. 2000.

[26] T. Sato *et al.*, "Nearly 4-inch-diameter

free-standing GaN wafer fabricated by hydride vapor phase epitaxy with pit-inducing buffer layer," *Jpn. J. Appl. Phys.*, vol. 52, no. 8S, May 2013, Art. no. 08JA08.
[27] H. Fujikura, T. Yoshida, M. Shibata, and Y. Otoki, "Recent progress of high-quality GaN substrates by HVPE method," in *Proc. Gallium Nitride Mater. Devices XII*, San Francisco, CA, USA, Feb. 2017, Art. no. 1010403.
[28] S. B. Reese, T. Remo, J. Green, and A. Zakutayev, "How much will gallium oxide power electronics cost?" *Joule*, vol. 3, no. 4, pp. 903–907, Apr. 2019.
[29] A. Tanaka, W. Choi, R. Chen, and S. A. Dayeh, "Si complies with GaN to overcome thermal mismatches for the heteroepitaxy of thick GaN on Si," *Adv. Mater.*, vol. 29, no. 38, 2017, Art. no. 1702557.
[30] K. J. Chen *et al.*, "GaN-on-Si power technology: Devices and applications," *IEEE Trans. Electron Devices*, vol. 64, no. 3, pp. 779–795, Mar. 2017.
[31] Y. Zhang, M. Yuan, N. Chowdhury, K. Cheng, and T. Palacios, "720-V/0.35-m$\Omega\cdot$cm^2 fully vertical GaN-on-Si power diodes by selective removal of Si substrates and buffer layers," *IEEE Electron Device Lett.*, vol. 39, no. 5, pp. 715–718, May 2018.
[32] D. C. Zhou *et al.*, "A massive adoption ready 200 mm 40 V-650 V E-mode GaN-on-Si power HEMTs technology," in *Proc. IEEE Appl. Power Electron. Conf. Expo. (APEC)*, New Orleans, LA, USA, Mar. 2020, pp. 636–639.
[33] S. Banerjee *et al.*, "Manufacturable and rugged 1.2 KV SiC MOSFETs fabricated in high-volume 150 mm CMOS fab," in *Proc. 28th Int. Symp. Power Semiconductor Devices ICs (ISPSD)*, Prague, Czech Republic, Jun. 2016, pp. 279–282.
[34] T. Kimoto and J. A. Cooper, *Fundamentals of Silicon Carbide Technology: Growth, Characterization, Devices, and Applications*. Singapore: Wiley, 2014.
[35] F. Dahlquist, "Junction barrier Schottky rectifiers in silicon carbide," M.S. thesis, KTH Roy. Inst. Technol., Stockholm, Sweden, 2002.
[36] H. Niwa, J. Suda, and T. Kimoto, "21.7 kV 4H-SiC PiN diode with a space-modulated junction termination extension," *Appl. Phys. Exp.*, vol. 5, no. 6, May 2012, Art. no. 064001.
[37] Z. Liu *et al.*, "High-voltage vertical GaN-on-GaN Schottky barrier diode using fluorine ion implantation treatment," *AIP Adv.*, vol. 9, no. 5, May 2019, Art. no. 055016.
[38] X. Zhang, X. Zou, X. Lu, C. W. Tang, and K. M. Lau, "Fully-and quasi-vertical GaN-on-Si p-i-n diodes: High performance and comprehensive comparison," *IEEE Trans. Electron Devices*, vol. 64, no. 3, pp. 809–815, Mar. 2017.
[39] M. Zhu *et al.*, "1.9-kV AlGaN/GaN lateral Schottky barrier diodes on silicon," *IEEE Electron Device Lett.*, vol. 36, no. 4, pp. 375–377, Apr. 2015.
[40] B. J. Baliga, "Power semiconductor device figure of merit for high-frequency applications," *IEEE Electron Device Lett.*, vol. 10, no. 10, pp. 455–457, Oct. 1989.
[41] H. M. McGlothlin, D. T. Morisette, J. A. Cooper, and M. R. Melloch, "4 kV silicon carbide Schottky diodes for high-frequency switching applications," in *57th Annu. Device Res. Conf. Dig.*, Santa Barbara, CA, USA, Jun. 1999, pp. 42–43.
[42] T. Zhang *et al.*, "A > 3 kV/2.94 m$\Omega\cdot$cm^2 and low leakage current with low turn-on voltage lateral GaN Schottky barrier diode on silicon substrate with anode engineering technique," *IEEE Electron Device Lett.*, vol. 40, no. 10, pp. 1583–1586, Oct. 2019.
[43] H. Ohta *et al.*, "Vertical GaN p-n junction diodes with high breakdown voltages over 4 kV," *IEEE Electron Device Lett.*, vol. 36, no. 11, pp. 1180–1182, Nov. 2015.
[44] T. Duong *et al.*, "Comparison of 4.5 kV SiC JBS and Si PiN diodes for 4.5 kV Si IGBT anti-parallel diode applications," in *Proc. 26th Annu. IEEE Appl. Power Electron. Conf. Expo. (APEC)*, Fort Worth, TX, USA, Mar. 2011, pp. 1057–1063.
[45] J. Spitz, M. R. Melloch, J. A. Cooper, and M. A. Capano, "2.6 kV 4H-SiC lateral DMOSFETs," *IEEE Electron Device Lett.*, vol. 19, no. 4, pp. 100–102, Apr. 1998.
[46] J. A. Cooper, M. R. Melloch, R. Singh, A. Agarwal, and J. W. Palmour, "Status and prospects for SiC power MOSFETs," *IEEE Trans. Electron Devices*, vol. 49, no. 4, pp. 658–664, Apr. 2002.
[47] J. B. Casady *et al.*, "New generation 10 kV SiC power MOSFET and diodes for industrial applications," in *Proc. PCIM Eur.*, Nuremberg, Germany, May 2015, pp. 1–8.
[48] M. Treu *et al.*, "Strategic considerations for unipolar SiC switch options: JFET vs. MOSFET," in *Proc. IEEE Ind. Appl. Annu. Meeting*, New Orleans, LA, USA, Sep. 2007, pp. 324–330.
[49] R. Barr *et al.* (2018). *High Voltage GaN Switch Reliability*. Accessed: Aug. 7, 2020. [Online]. Available: https://www.transphormusa.com/en/document/high-voltage-gan-switch-reliability/
[50] R. A. Khadar, C. Liu, R. Soleimanzadeh, and E. Matioli, "Fully vertical GaN-on-Si power MOSFETs," *IEEE Electron Device Lett.*, vol. 40, no. 3, pp. 443–446, Mar. 2019.
[51] D. Biswas, N. Torii, K. Yamamoto, and T. Egawa, "Demonstration of fully-vertical GaN-on-Si power MOSFETs using regrowth technique," *Electron. Lett.*, vol. 55, no. 7, pp. 404–406, Apr. 2019.
[52] T. P. Chow *et al.*, "SiC and GaN bipolar power devices," *Solid-State Electron.*, vol. 44, no. 2, pp. 277–301, Feb. 2000.
[53] D. C. Sheridan, A. Ritenour, V. Bondarenko, P. Burks, and J. B. Casady, "Record 2.8 mΩ-cm^2 1.9 kV enhancement-mode SiC VJFETs," in *Proc. 21st Int. Symp. Power Semiconductor Devices IC's*, Barcelona, Spain, Jun. 2009, pp. 335–338.
[54] S. Sabri *et al.*, "New generation 6.5 kV SiC power MOSFET," in *Proc. IEEE 5th Workshop Wide Bandgap Power Devices Appl. (WiPDA)*, Albuquerque, NM, USA, Oct. 2017, pp. 246–250.
[55] I. Hwang *et al.*, "1.6 kV, 2.9 mΩcm^2 normally-off p-GaN HEMT device," in *Proc. 24th Int. Symp. Power Semiconductor Devices ICs*, Bruges, Belgium, Jun. 2012, pp. 41–44.
[56] C.-H. Wu *et al.*, "Normally-off tri-gate GaN MIS-HEMTs with 0.76 m$\Omega\cdot$cm^2 specific on-resistance for power device applications," *IEEE Trans. Electron Devices*, vol. 66, no. 8, pp. 3441–3446, Aug. 2019.
[57] M. Sun, Y. Zhang, X. Gao, and T. Palacios, "High-performance GaN vertical fin power transistors on bulk GaN substrates," *IEEE Electron Device Lett.*, vol. 38, no. 4, pp. 509–512, Apr. 2017.
[58] J. Zhang, P. Alexandrov, T. Burke, and J. H. Zhao, "4H-SiC power bipolar junction transistor with a very low specific ON-resistance of 2.9 m$\Omega\cdot$cm^2," *IEEE Electron Device Lett.*, vol. 27, no. 5, pp. 368–370, May 2006.
[59] S. H. Ryu *et al.*, "Development of 15 kV 4H-SiC IGBTs," *Mater. Sci. Forum*, vols. 717–720, pp. 1135–1138, May 2012.
[60] L. Cheng *et al.*, "20 kV, 2 cm^2, 4H-SiC gate turn-off thyristors for advanced pulsed power applications," in *Proc. 19th IEEE Pulsed Power Conf. (PPC)*, San Francisco, CA, USA, Jun. 2013, pp. 1–4.
[61] J. W. Palmour, J. Q. Zhang, M. K. Das, R. Callanan, A. K. Agarwal, and D. E. Grider, "SiC power devices for smart grid systems," in *Proc. Int. Power Electron. Conf. ECCE ASIA*, Sapporo, Japan, Jun. 2010, pp. 1006–1013.
[62] T. Fujihira, "Theory of semiconductor superjunction devices," *Jpn. J. Appl. Phys.*, vol. 36, no. 10, pp. 6254–6262, Oct. 1997.
[63] R. Kosugi *et al.*, "First experimental demonstration of SiC super-junction (SJ) structure by multi-epitaxial growth method," in *Proc. IEEE 26th Int. Symp. Power Semiconductor Devices IC's (ISPSD)*, Waikoloa, HI, USA, Jun. 2014, pp. 346–349.
[64] T. Masuda, Y. Saito, T. Kumazawa, T. Hatayama, and S. Harada, "0.63 mΩcm^2/1170 V 4H-SiC super junction V-groove trench MOSFET," in *IEDM Tech. Dig.*, San Francisco, CA, USA, Dec. 2018, pp. 8.1.1–8.1.4.
[65] Y. Ma, M. Xiao, R. Zhang, H. Wang, and Y. Zhang, "Superjunction power transistors with interface charges: A case study for GaN," *IEEE J. Electron Devices Soc.*, vol. 8, pp. 42–48, 2020.
[66] X. Huang, Z. Liu, F. C. Lee, and Q. Li, "Characterization and enhancement of high-voltage cascode GaN devices," *IEEE Trans. Electron Devices*, vol. 62, no. 2, pp. 270–277, Feb. 2015.
[67] E. Persson. *CoolGaNTM Application Note*. Accessed: Jun. 25, 2020. [Online]. Available: https://www.infineon.com/dgdl/Infineon-ApplicationNote_CoolGaN_600V_emode_HEMTs-AN-v01_00-EN.pdf?fileId=5546d46262b31d2e016368e4cab10701
[68] R. Rupp, M. Treu, S. Voss, F. Bjork, and T. Reimann, "'2nd generation' SiC Schottky diodes: A new benchmark in SiC device ruggedness," in *Proc. IEEE Int. Symp. Power Semiconductor Devices IC's*, Naples, Italy, Jun. 2006, pp. 1–4.
[69] T.-T. Nguyen, A. Ahmed, T. V. Thang, and J.-H. Park, "Gate oxide reliability issues of SiC MOSFETs under short-circuit operation," *IEEE Trans. Power Electron.*, vol. 30, no. 5, pp. 2445–2455, May 2015.
[70] J. Wang and X. Jiang, "Review and analysis of SiC MOSFETs' ruggedness and reliability," *IET Power Electron.*, vol. 13, no. 3, pp. 445–455, Feb. 2020.
[71] J. Liu, G. Zhang, B. Wang, W. Li, and J. Wang, "Gate failure physics of SiC MOSFETs under short-circuit stress," *IEEE Electron Device Lett.*, vol. 41, no. 1, pp. 103–106, Jan. 2020.
[72] N. Badawi, A. E. Awwad, and S. Dieckerhoff, "Robustness in short-circuit mode: Benchmarking of 600 V GaN HEMTs with power Si and SiC MOSFETs," in *Proc. IEEE Energy Convers. Congr. Expo. (ECCE)*, Milwaukee, WI, USA, Sep. 2016, pp. 1–7.
[73] P. Xue, L. Maresca, M. Riccio, G. Breglio, and A. Irace, "Investigation on the short-circuit oscillation of cascode GaN HEMTs," *IEEE Trans. Power Electron.*, vol. 35, no. 6, pp. 6292–6300, Jun. 2020.
[74] S. Ji *et al.*, "Short-circuit characterization and protection of 10-kV SiC MOSFET," *IEEE Trans. Power Electron.*, vol. 34, no. 2, pp. 1755–1764, Feb. 2019.
[75] G. Romano *et al.*, "A comprehensive study of short-circuit ruggedness of silicon carbide power MOSFETs," *IEEE J. Emerg. Sel. Topics Power Electron.*, vol. 4, no. 3, pp. 978–987, Sep. 2016.
[76] D. J. Lichtenwalner *et al.*, "Reliability studies of SiC vertical power MOSFETs," in *Proc. IEEE Int. Rel. Phys. Symp. (IRPS)*, Burlingame, CA, USA, Mar. 2018, pp. 2B.2-1–2B.2-6.
[77] R. Strittmatter, C. Zhou, A. Lidow, and Y. Ma, "Enhancement mode gallium nitride transistor reliability," in *Proc. IEEE Appl. Power Electron. Conf. Expo. (APEC)*, Charlotte, NC, USA, Mar. 2015, pp. 1409–1413.
[78] Z. Ni, X. Lyu, O. P. Yadav, B. N. Singh, S. Zheng, and D. Cao, "Overview of real-time lifetime prediction and extension for SiC power converters," *IEEE Trans. Power Electron.*, vol. 35, no. 8, pp. 7765–7794, Aug. 2020.
[79] J. O. Gonzalez, R. Wu, S. Jahdi, and O. Alatise, "Performance and reliability review of 650 V and 900 V silicon and SiC devices: MOSFETs, cascode JFETs and IGBTs," *IEEE Trans. Ind. Electron.*, vol. 67, no. 9, pp. 7375–7385, Sep. 2020.
[80] G. Meneghesso *et al.*, "Reliability of GaN high-electron-mobility transistors: State of the art and perspectives," *IEEE Trans. Device Mater. Rel.*, vol. 8, no. 2, pp. 332–343, Jun. 2008.
[81] J. A. del Alamo and E. S. Lee, "Stability and reliability of lateral GaN power field-effect transistors," *IEEE Trans. Electron Devices*, vol. 66, no. 11, pp. 4578–4590, Nov. 2019.
[82] L. C. Yu, G. T. Dunne, K. S. Matocha, K. P. Cheung, J. S. Suehle, and K. Sheng, "Reliability issues of SiC MOSFETs: A technology for high-temperature environments," *IEEE Trans. Device Mater. Rel.*, vol. 10, no. 4, pp. 418–426, Dec. 2010.
[83] A. Khaligh and M. D'Antonio, "Global trends in

high-power on-board chargers for electric vehicles," *IEEE Trans. Veh. Technol.*, vol. 68, no. 4, pp. 3306–3324, Apr. 2019.

[84] M. Y. Metwly, M. S. Abdel-Majeed, A. S. Abdel-Khalik, R. A. Hamdy, M. S. Hamad, and S. Ahmed, "A review of integrated on-board EV battery chargers: Advanced topologies, recent developments and optimal selection of FSCW slot/pole combination," *IEEE Access*, vol. 8, pp. 85216–85242, 2020.

[85] Z. Liu, B. Li, F. C. Lee, and Q. Li, "High-efficiency high-density critical mode rectifier/inverter for WBG-device-based on-board charger," *IEEE Trans. Ind. Electron.*, vol. 64, no. 11, pp. 9114–9123, Nov. 2017.

[86] D. S. Gautam, F. Musavi, M. Edington, W. Eberle, and W. G. Dunford, "An automotive onboard 3.3-kW battery charger for PHEV application," *IEEE Trans. Veh. Technol.*, vol. 61, no. 8, pp. 3466–3474, Oct. 2012.

[87] B. Whitaker *et al.*, "A high-density, high-efficiency, isolated on-board vehicle battery charger utilizing silicon carbide power devices," *IEEE Trans. Power Electron.*, vol. 29, no. 5, pp. 2606–2617, May 2014.

[88] L. Huber, Y. Jang, and M. M. Jovanovic, "Performance evaluation of bridgeless PFC boost rectifiers," *IEEE Trans. Power Electron.*, vol. 23, no. 3, pp. 1381–1390, May 2008.

[89] L. Zhou, Y. Wu, J. Honea, and Z. Wang, "High-efficiency true bridgeless totem pole PFC based on GaN HEMT: Design challenges and cost-effective solution," in *Proc. PCIM Eur.*, Nuremberg, Germany, May 2015, pp. 1–8.

[90] Q. Huang, R. Yu, Q. Ma, and A. Q. Huang, "Predictive ZVS control with improved ZVS time margin and limited variable frequency range for a 99% efficient, 130-W/in^3 MHz GaN totem-pole PFC rectifier," *IEEE Trans. Power Electron.*, vol. 34, no. 7, pp. 7079–7091, Jul. 2019.

[91] X. Wang, C. Jiang, B. Lei, H. Teng, H. K. Bai, and J. L. Kirtley, "Power-loss analysis and efficiency maximization of a silicon-carbide MOSFET-based three-phase 10-kW bidirectional EV charger using variable-DC-bus control," *IEEE J. Emerg. Sel. Topics Power Electron.*, vol. 4, no. 3, pp. 880–892, Sep. 2016.

[92] G. Yang, E. Draugedalen, T. Sorsdahl, H. Liu, and R. Lindseth, "Design of high efficiency high power density 10.5 kW three phase on-board-charger for electric/hybrid vehicles," in *Proc. PCIM Eur.*, Nuremberg, Germany, May 2016, pp. 1–7.

[93] H.-N. Vu, M. Abdel-Monem, M. El Baghdadi, J. Van Mierlo, and O. Hegazy, "Multi-objective optimization of on-board chargers based on state-of-the-art 650 V GaN power transistors for the application of electric vehicles," in *Proc. IEEE Vehicle Power Propuls. Conf. (VPPC)*, Hanoi, Vietnam, Oct. 2019, pp. 1–6.

[94] S. Endres, C. Sessler, S. Zeltner, B. Eckardt, and T. Morita, "6 kW bidirectional, insulated on-board charger with normally-off GaN gate injection transistors," in *Proc. PCIM Eur.*, Nuremberg, Germany, May 2017, pp. 1–6.

[95] M. Gaertner, D. Cavallaro, M. Pulvirenti, E. Zanetti, M. Saggio, and M. Ferrara, "SiC MOSFETs as enabler for the future ePowertrain and its behaviour under short circuit condition," in *Proc. AEIT Int. Conf. Electr. Electron. Technol. Automot. (AEIT AUTOMOTIVE)*, Turin, Italy, Jul. 2019, pp. 1–5.

[96] A. Taylor, J. Lu, L. Zhu, K. Bai, M. McAmmond, and A. Brown, "Comparison of SiC MOSFET-based and GaN HEMT-based high-efficiency high-power-density 7.2 kW EV battery chargers," *IET Power Electron.*, vol. 11, no. 11, pp. 1849–1857, 2018.

[97] H. Tu, H. Feng, S. Srdic, and S. Lukic, "Extreme fast charging of electric vehicles: A technology overview," *IEEE Trans. Transport. Electrific.*, vol. 5, no. 4, pp. 861–878, Dec. 2019.

[98] D. Aggeler, F. Canales, H. Z.-D. La Parra, A. Coccia, N. Butcher, and O. Apeldoorn, "Ultra-fast DC-charge infrastructures for EV-mobility and future smart grids," in *Proc. IEEE PES Innov. Smart Grid Technol. Conf. Eur. (ISGT Europe)*, Gothenburg, Sweden, Oct. 2010, pp. 1–8.

[99] L. Tan, B. Wu, S. Rivera, and V. Yaramasu, "Comprehensive DC power balance management in high-power three-level DC–DC converter for electric vehicle fast charging," *IEEE Trans. Power Electron.*, vol. 31, no. 1, pp. 89–100, Jan. 2016.

[100] C. Zhu. *High-Efficiency, Medium-Voltage-Input, Solid-State-Transformer-Based 400-kW/1000-V/400-A Extreme Fast Charger for Electric Vehicles*. Accessed: Aug. 4, 2020. [Online]. Available: https://www.energy.gov/sites/prod/files/2019/06/f64/elt241_zhu_2019_o_4.24_9.31pm_jl.pdf

[101] A. Moeini and S. Wang, "Design of fast charging technique for electrical vehicle charging stations with grid-tied cascaded H-bridge multilevel converters," in *Proc. IEEE Appl. Power Electron. Conf. Expo. (APEC)*, San Antonio, TX, USA, Mar. 2018, pp. 3583–3590.

[102] A. C. Nair and B. G. Fernandes, "A solid state transformer based fast charging station for all categories of electric vehicles," in *Proc. 44th Annu. Conf. IEEE Ind. Electron. Soc. (IECON)*, Washington, DC, USA, Oct. 2018, pp. 1989–1994.

[103] J. E. Huber, J. Böhler, D. Rothmund, and J. W. Kolar, "Analysis and cell-level experimental verification of a 25 kW all-SiC isolated front end 6.6 kV/400 V AC-DC solid-state transformer," *CPSS Trans. Power Electron. Appl.*, vol. 2, no. 2, pp. 140–148, Jun. 2017.

[104] S. Srdic, X. Liang, C. Zhang, W. Yu, and S. Lukic, "A SiC-based high-performance medium-voltage fast charger for plug-in electric vehicles," in *Proc. IEEE Energy Convers. Congr. Expo. (ECCE)*, Milwaukee, WI, USA, Sep. 2016, pp. 1–6.

[105] J.-S. Lai, W.-H. Lai, S.-R. Moon, L. Zhang, and A. Maitra, "A 15-kV class intelligent universal transformer for utility applications," in *Proc. IEEE Appl. Power Electron. Conf. Expo. (APEC)*, Long Beach, CA, USA, Mar. 2016, pp. 1974–1981.

[106] F. Wang, G. Wang, A. Huang, W. Yu, and X. Ni, "Design and operation of a 3.6 kV high performance solid state transformer based on 13 kV SiC MOSFET and JBS diode," in *Proc. IEEE Energy Convers. Congr. Expo. (ECCE)*, Pittsburgh, PA, USA, Sep. 2014, pp. 4553–4560.

[107] S. Madhusoodhanan *et al.*, "Solid-state transformer and MV grid tie applications enabled by 15 kV SiC IGBTs and 10 kV SiC MOSFETs based multilevel converters," *IEEE Trans. Ind. Appl.*, vol. 51, no. 4, pp. 3343–3360, Aug. 2015.

[108] D. Rothmund, T. Guillod, D. Bortis, and J. W. Kolar, "99.1% efficient 10 kV SiC-based medium-voltage ZVS bidirectional single-phase PFC AC/DC stage," *IEEE J. Emerg. Sel. Topics Power Electron.*, vol. 7, no. 2, pp. 779–797, Jun. 2019.

[109] D. Rothmund, T. Guillod, D. Bortis, and J. W. Kolar, "99% efficient 10 kV SiC-based 7 kV/400 V DC transformer for future data centers," *IEEE J. Emerg. Sel. Topics Power Electron.*, vol. 7, no. 2, pp. 753–767, Jun. 2019.

[110] A. Maitra, S. Rajagopalan, J.-S. Lai, M. DuVall, and M. McGranaghan, "Medium voltage stand alone DC fast charger," U.S. Patent 20 130 134 935 A1, May 30, 2013.

[111] F. Lu, H. Zhang, H. Hofmann, and C. Mi, "A double-sided LCLC-compensated capacitive power transfer system for electric vehicle charging," *IEEE Trans. Power Electron.*, vol. 30, no. 11, pp. 6011–6014, Nov. 2015.

[112] S. Li, W. Li, J. Deng, T. D. Nguyen, and C. C. Mi, "A double-sided LCC compensation network and its tuning method for wireless power transfer," *IEEE Trans. Veh. Technol.*, vol. 64, no. 6, pp. 2261–2273, Jun. 2015.

[113] D. Patil, M. K. McDonough, J. M. Miller, B. Fahimi, and P. T. Balsara, "Wireless power transfer for vehicular applications: Overview and challenges," *IEEE Trans. Transport. Electrific.*, vol. 4, no. 1, pp. 3–37, Mar. 2018.

[114] A. Kurs, A. Karalis, R. Moffatt, J. D. Joannopoulos, P. Fisher, and M. Soljačić, "Wireless power transfer via strongly coupled magnetic resonances," *Science*, vol. 317, no. 5834, pp. 83–86, Jul. 2007.

[115] R. Bosshard, U. Iruretagoyena, and J. W. Kolar, "Comprehensive evaluation of rectangular and double-D coil geometry for 50 kW/85 kHz IPT system," *IEEE J. Emerg. Sel. Topics Power Electron.*, vol. 4, no. 4, pp. 1406–1415, Dec. 2016.

[116] R. Bosshard, J. W. Kolar, J. Mühlethaler, I. Stevanović, B. Wunsch, and F. Canales, "Modeling and η-α-Pareto optimization of inductive power transfer coils for electric vehicles," *IEEE J. Emerg. Sel. Topics Power Electron.*, vol. 3, no. 1, pp. 50–64, Mar. 2015.

[117] W. Li, H. Zhao, S. Li, J. Deng, T. Kan, and C. C. Mi, "Integrated LCC compensation topology for wireless charger in electric and plug-in electric vehicles," *IEEE Trans. Ind. Electron.*, vol. 62, no. 7, pp. 4215–4225, Dec. 2015.

[118] T. Kan, T.-D. Nguyen, J. C. White, R. K. Malhan, and C. C. Mi, "A new integration method for an electric vehicle wireless charging system using LCC compensation topology: Analysis and design," *IEEE Trans. Power Electron.*, vol. 32, no. 2, pp. 1638–1650, Feb. 2017.

[119] J. M. Miller, O. C. Onar, and M. Chinthavali, "Primary-side power flow control of wireless power transfer for electric vehicle charging," *IEEE J. Emerg. Sel. Topics Power Electron.*, vol. 3, no. 1, pp. 147–162, Mar. 2015.

[120] Y. Tang, Y. Chen, U. K. Madawala, D. J. Thrimawithana, and H. Ma, "A new controller for bidirectional wireless power transfer systems," *IEEE Trans. Power Electron.*, vol. 33, no. 10, pp. 9076–9087, Oct. 2018.

[121] V. P. Galigekere *et al.*, "Design and implementation of an optimized 100 kW stationary wireless charging system for EV battery recharging," in *Proc. IEEE Energy Convers. Congr. Expo. (ECCE)*, Portland, OR, USA, Sep. 2018, pp. 3587–3592.

[122] G. Zhu and R. D. Lorenz, "Achieving low magnetic flux density and low electric field intensity for a loosely coupled inductive wireless power transfer system," *IEEE Trans. Ind. Appl.*, vol. 54, no. 6, pp. 6383–6393, Nov. 2018.

[123] D. H. Tran, V. B. Vu, and W. Choi, "Design of a high-efficiency wireless power transfer system with intermediate coils for the on-board chargers of electric vehicles," *IEEE Trans. Power Electron.*, vol. 33, no. 1, pp. 175–187, Jan. 2018.

[124] J. Choi, D. Tsukiyama, Y. Tsuruda, and J. M. R. Davila, "High-frequency, high-power resonant inverter with eGaN FET for wireless power transfer," *IEEE Trans. Power Electron.*, vol. 33, no. 3, pp. 1890–1896, Mar. 2018.

[125] S. Li and C. C. Mi, "Wireless power transfer for electric vehicle applications," *IEEE J. Emerg. Sel. Topics Power Electron.*, vol. 3, no. 1, pp. 4–17, Mar. 2015.

[126] C. Liu, A. P. Hu, B. Wang, and N.-K.-C. Nair, "A capacitively coupled contactless matrix charging platform with soft switched transformer control," *IEEE Trans. Ind. Electron.*, vol. 60, no. 1, pp. 249–260, Jan. 2013.

[127] J. Dai and D. C. Ludois, "A survey of wireless power transfer and a critical comparison of inductive and capacitive coupling for small gap applications," *IEEE Trans. Power Electron.*, vol. 30, no. 11, pp. 6017–6029, Nov. 2015.

[128] C. Liu, A. P. Hu, G. A. Covic, and N.-K.-C. Nair, "Comparative study of CCPT systems with two different inductor tuning positions," *IEEE Trans. Power Electron.*, vol. 27, no. 1, pp. 294–306, Jan. 2012.

[129] L. Li, Z. Wang, F. Gao, S. Wang, and J. Deng, "A family of compensation topologies for capacitive power transfer converters for wireless electric vehicle charger," *Appl. Energy*, vol. 260, Feb. 2020, Art. no. 114156.

[130] S. Li, Z. Liu, H. Zhao, L. Zhu, C. Shuai, and Z. Chen, "Wireless power transfer by electric field resonance and its application in dynamic charging," *IEEE Trans. Ind. Electron.*, vol. 63, no. 10, pp. 6602–6612, Oct. 2016.

[131] H. Zhang, F. Lu, H. Hofmann, W. Liu, and C. C. Mi, "Six-plate capacitive coupler to reduce electric field emission in large air-gap capacitive power transfer," *IEEE Trans. Power Electron.*,

vol. 33, no. 1, pp. 665–675, Jan. 2018.
[132] H. Zhang, C. Zhu, and F. Lu, "Long-distance and high-power capacitive power transfer based on the double-sided LC compensation: Analysis and design," in *Proc. IEEE Transp. Electrific. Conf. Expo (ITEC)*, Detroit, MI, USA, Jun. 2019, pp. 1–5.
[133] B. Luo, L. Xu, T. Long, Y. Xu, R. Mai, and Z. He, "An LC-CLC compensated CPT system to achieve the maximum power transfer for high power applications," in *Proc. IEEE Appl. Power Electron. Conf. Expo. (APEC)*, New Orleans, LA, USA, Mar. 2020, pp. 3186–3189.
[134] H. Zhang, F. Lu, and C. Mi, "An electric roadway system leveraging dynamic capacitive wireless charging: Furthering the continuous charging of electric vehicles," *IEEE Electrific. Mag.*, vol. 8, no. 2, pp. 52–60, Jun. 2020.
[135] A. Q. Cai and L. Siek, "A 2-kW, 95% efficiency inductive power transfer system using gallium nitride gate injection transistors," *IEEE J. Emerg. Sel. Topics Power Electron.*, vol. 5, no. 1, pp. 458–468, Mar. 2017.
[136] C. Nagai *et al.*, "Scaling law of coupling coefficient and coil size in wireless power transfer design via magnetic coupling," *Electr. Eng. Jpn.*, vol. 202, no. 4, pp. 21–30, Mar. 2018.
[137] H. Zhang, F. Lu, H. Hofmann, W. Liu, and C. C. Mi, "A four-plate compact capacitive coupler design and LCL-compensated topology for capacitive power transfer in electric vehicle charging application," *IEEE Trans. Power Electron.*, vol. 31, no. 12, pp. 8541–8551, Dec. 2016.
[138] S. Sinha, B. Regensburger, A. Kumar, and K. Afridi, "A very-high-power-transfer-density GaN-based capacitive wireless power transfer system," in *Proc. IEEE 5th Workshop Wide Bandgap Power Devices Appl. (WiPDA)*, Albuquerque, NM, USA, Oct. 2017, pp. 360–365.
[139] B. Regensburger, A. Kumar, S. Sinha, and K. Afridi, "High-performance 13.56-MHz large air-gap capacitive wireless power transfer system for electric vehicle charging," in *Proc. IEEE 19th Workshop Control Modeling Power Electron. (COMPEL)*, Padua, Italy, Jun. 2018, pp. 1–4.
[140] B. Regensburger, J. Estrada, A. Kumar, S. Sinha, Z. Popović, and K. K. Afridi, "High-performance capacitive wireless power transfer system for electric vehicle charging with enhanced coupling plate design," in *Proc. IEEE Energy Convers. Congr. Expo. (ECCE)*, Portland, OR, USA, Sep. 2018, pp. 2472–2477.
[141] B. Regensburger, S. Sinha, A. Kumar, J. Vance, Z. Popovic, and K. K. Afridi, "Kilowatt-scale large air-gap multi-modular capacitive wireless power transfer system for electric vehicle charging," in *Proc. IEEE Appl. Power Electron. Conf. Expo. (APEC)*, San Antonio, TX, USA, Mar. 2018, pp. 666–671.
[142] B. Regensburger, S. Sinha, A. Kumar, S. Maji, and K. K. Afridi, "High-performance multi-MHz capacitive wireless power transfer system for EV charging utilizing interleaved-foil coupled inductors," *IEEE J. Emerg. Sel. Topics Power Electron.*, early access, Oct. 13, 2020, doi: 10.1109/JESTPE.2020.3030757.
[143] B. Regensburger, A. Kumar, S. Sinha, J. Xu, and K. K. Afridi, "High-efficiency high-power-transfer-density capacitive wireless power transfer system for electric vehicle charging utilizing semi-toroidal interleaved-foil coupled inductors," in *Proc. IEEE Appl. Power Electron. Conf. Expo. (APEC)*, Anaheim, CA, USA, Mar. 2019, pp. 1533–1538.
[144] B. Li, Q. Li, F. C. Lee, Z. Liu, and Y. Yang, "A high-efficiency high-density wide-bandgap device-based bidirectional on-board charger," *IEEE J. Emerg. Sel. Topics Power Electron.*, vol. 6, no. 3, pp. 1627–1636, Sep. 2018.

ABOUT THE AUTHORS

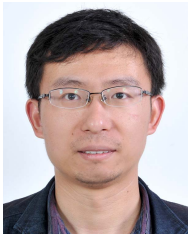

Siqi Li (Member, IEEE) received the B.S. and Ph.D. degrees in electrical engineering from Tsinghua University, Beijing, China, in 2004 and 2010, respectively.

He was a Postdoctoral Fellow with the University of Michigan, Dearborn, MI, USA, from 2011 to 2013. He was a Visiting Scholar with San Diego State University, San Diego, CA, USA, from 2018 to 2019. In 2013, he joined the Faculty of Electric Power Engineering, Kunming University of Science and Technology (KUST), Kunming, China, where he is currently a Professor with the Department of Electrical Engineering. He is also the Director of the Advanced Power Electronics and New Energy Laboratory, KUST. His research interest focuses on battery management systems, high-performance wired, wireless battery chargers for electric vehicles, and solid-state transformers.

Sizhao Lu (Member, IEEE) received the B.S. and M.S. degrees in electrical engineering from the Harbin Institute of Technology, Harbin, China, in 2008 and 2010, respectively, and the Ph.D. degree in electrical engineering from Tsinghua University, Beijing, China, in 2016.

He became an Associate Professor at the Department of Electrical Engineering, Kunming University of Science and Technology, Kunming, China, in 2019. He was a Visiting Scholar with the Center for Power Electronics Systems, Virginia Tech, Blacksburg, VA, USA, from February 2012 to November 2013. His research interests include modular multilevel converters (MMCs), solid-state transformers, and high-frequency high-power three-level dc–dc converters.

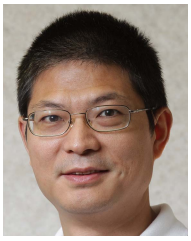

Chunting Chris Mi (Fellow, IEEE) received the B.S.E.E. and M.S.E.E. degrees in electrical engineering from Northwestern Polytechnical University, Xi'an, China, in 1985 and 1988, respectively, and the Ph.D. degree in electrical engineering from the University of Toronto, Toronto, ON, Canada, in 2001.

He was with the University of Michigan, Dearborn, MI, USA, from 2001 to 2015. He is currently a Professor, the Chair of electrical and computer engineering, and the Director of the Department of Energy (DOE)-funded Graduate Automotive Technology Education (GATE) Center for Electric Drive Transportation, San Diego State University (SDSU), San Diego, CA, USA. His research interests include electric drives, power electronics, electric machines, electrical and hybrid vehicles, wireless power transfer, and power electronics.

Dr. Mi is a Fellow of the Society of Automotive Engineers (SAE). He was a recipient of the IEEE PELS Emerging Technology Award in 2019, the IEEE Transactions on Power Electronics Best Paper Award, and two IEEE Transactions on Power Electronics Prize Letter Awards.